Journal of Nanobiotechnology

RESEARCH

Open Access

Spatial and cellular composition of lung fibrosis induced by multi-walled carbon nanotubes

Biqi Han[1], Xinwei Li[2], Jiayi Li[1], Yunfeng Liu[1], Siyu Li[3], Jiawen Tian[1], Zhanjun Lv[1], Dongfang Liu[1], Miaomiao Li[1], Shuke Ji[1], Jingjing Lu[1] and Zhigang Zhang[1*]

Abstract

Background The pulmonary immune system orchestrates lung homeostasis and protects against environmental insults through coordinated actions of immune and structural cells. Traditional Chinese medicine recognized the functional interaction between the lungs and the large intestine more than 2000 years ago, but direct evidence for this relationship in modern biomedical research remains limited. Although inhaled nanomaterials can induce lung fibrosis, the underlying immune mechanisms and their impact on large intestine remain poorly understood. Here, we integrated spatial transcriptomics, mRNA-seq, metabolomics, microbiome profiling, and validation in vitro to investigate how multi-walled carbon nanotubes (MWCNTs) exposure affects pulmonary immune responses and gut homeostasis in mice.

Results MWCNTs were administered to mice via oropharyngeal aspiration. We integrated spatial transcriptomics, bulk RNA sequencing, serum metabolomics, 16S rRNA microbiome profiling, and macrophage experiments in vitro. This multi-omics approach mapped pulmonary cellular alterations, identified key cell–cell signaling pathways, and examined downstream metabolic and intestinal changes provoked by MWCNTs. The results suggested that inhaled MWCNTs induced distinct spatial reorganization of pulmonary cellular architecture, characterized by macrophage- and fibroblast-enriched clusters associated with localized immune activation. Furthermore, cell–cell communication analysis identified Slamf7–Slamf7 interactions as key drivers of macrophage superactivation evidenced by excessive pro-inflammatory cytokine release. Notably, knockdown of Slamf7 in alveolar macrophages in vitro effectively attenuated the superactivation. The macrophage superactivation altered serum metabolic profiles, particularly in pathways related to energy metabolism and inflammation. Finally, lung injury extended to the distal intestine, where rectal epithelial barrier integrity was compromised, resulting in microbial and metabolic imbalance.

Conclusion These findings highlight the hazardous potential of inhaled MWCNTs based on macrophage superactivation induced by Slamf7 in the lung, providing mechanistic evidence for the lung–gut link described in traditional Chinese medicine. Together, our results identify molecular targets to mitigate nanomaterial immunotoxicity and inform the design and using of safer, surface-engineered MWCNTs.

*Correspondence:
Zhigang Zhang
zhangzhigang@neau.edu.cn

Full list of author information is available at the end of the article

Keywords MWCNTs, Spatial transcriptomics, Macrophage superactivation, Slamf7, Lung-gut axis, Lung fibrosis

Graphical abstract

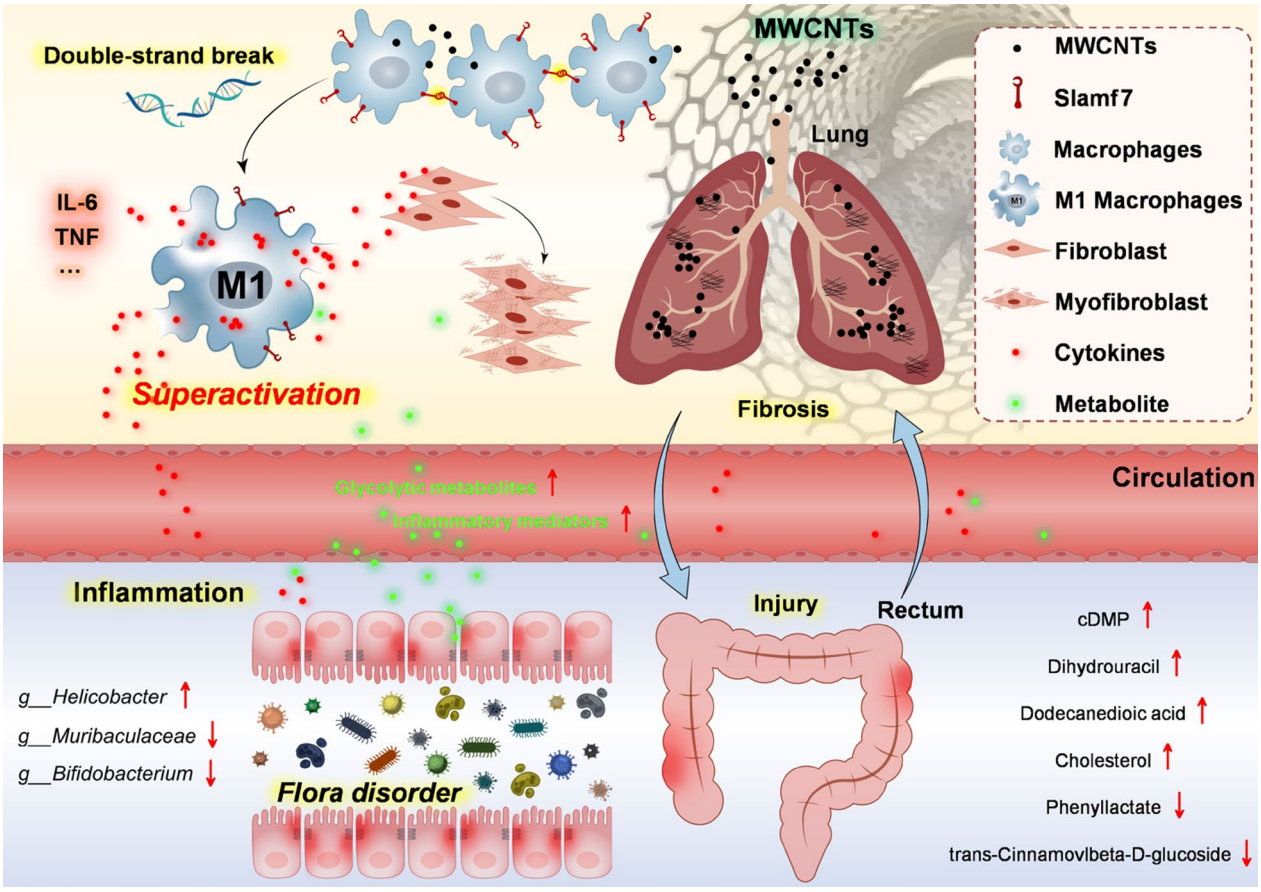

Introduction

The extraordinary mechanical, electrical, and thermal properties of carbon nanotubes (CNTs) have led to their widespread application in various fields, including composite materials, energy storage, medicine, and bioengineering [1]. Their exceptional tensile strength has particularly attracted attention for potential applications such as space elevator cables [2]. With global annual production exceeding 5000 tons, concerns regarding occupational and environmental exposure have been greatly intensified [3, 4]. Among CNT variants, multi-walled carbon nanotubes (MWCNTs) are particularly prevalent and have been implicated in adverse respiratory outcomes. Epidemiological and occupational studys have reported elevated oxidative stress markers, including GPx, SOD, and lipid peroxidation products in blood, sputum, and exhaled breath condensate of CNT-exposed workers [5, 6]. Notably, CNTs were identified in the dust at the 9/11 disaster site, where long-term responders developed respiratory diseases such as pulmonary fibrosis, chronic bronchiolitis, and granulomatosis [7]. In recognition of these risks, the IARC has classified MWCNT-7 as possibly carcinogenic to humans (Group 2B) [8].

The lung comprises a highly heterogeneous microenvironment, where epithelial, immune, and stromal cells interact dynamically to maintain pulmonary homeostasis [9]. Inhaled MWCNTs can disrupt the pulmonary homeostasis, leading to immune activation and tissue remodeling [10]. Although accumulating evidence links MWCNT exposure to lung fibrosis, the underlying cellular and molecular mechanisms remain poorly defined [11, 12]. Among pulmonary immune cells, macrophages act as early sentinels, recognizing foreign particles via scavenger receptors and initiating inflammatory cascades [13]. Upon activation, macrophages secrete pro-inflammatory cytokines that recruit additional immune cells and may exacerbate tissue injury [14]. Excessive or dysregulated macrophage responses are known contributors to fibrosis and have been associated with cytokine storm [15, 16]. However, most studies on MWCNT-induced pulmonary lesions have focused on limited pathways,

often overlooking spatial and cell-type-specific responses [17, 18]. To date, how MWCNTs reshape the pulmonary immune landscape and macrophage-driven fibrotic programs remains poorly defined.

The ancient Chinese recognized a special connection between the lungs and the intestines, constructing the theory of the "internal-external relationship between the lungs and large intestine" based on the principles of yin-yang and meridian [19]. From a modern biological perspective, both the lung and the intestine originate from the endoderm [20], and this shared embryonic provenance accounts for their numerous structural and functional parallels. In modern immunology, the lung–gut axis has emerged as a critical regulatory pathway through which local inflammation in one organ can influence immune responses and barrier function in the other [21–23]. Environmental toxicants are increasingly recognized to disrupt host metabolic and immune homeostasis, partly through alterations in gut microbial composition and metabolite production [24–27]. However, the influence of inhaled MWCNT on the lung–gut axis, particularly its effects on intestinal barrier integrity, microbiota composition, and host metabolism, remains poorly understood.

Here, we applied spatial and bulk transcriptomic techniques to delineate the spatial architecture and immune microenvironment of the lung following MWCNTs exposure, with particular focus on macrophage-mediated inflammatory and fibrotic responses. Integrated serum metabolomic profiling further identified characteristic metabolic signatures associated with pulmonary injury. Moreover, we investigated changes in gut microbiota composition and intestinal mucosal signaling, revealing the perturbations induced by mirror pulmonary immune activation. The results uncover a bidirectional interplay between the lung and gut under MWCNT challenge, and provide modern biological support for the traditional Chinese medicine concept of the "internal and external relationship between the lung and large intestine." These insights lay a scientific foundation for safer surface-engineering and targeted application strategies for CNTs in future biomedical or industrial use.

Materials and methods

Reagents and antibodies

10% F-68 solution was acquired from Gibco (Shanghai, China). MWCNTs of > 99.9 wt % purity, featuring a specific surface area greater than 70 m^2/g, an outer diameter of 30–50 nm, and lengths under 10 μm, were procured from Chengdu Organic Chemicals Co., Ltd. (Chengdu, China). Morphological assessment of the MWCNTs was performed with a field-emission scanning electron microscope (SU 8010, Hitachi, Japan). The aqueous dispersibility and surface charge of MWCNTs were characterized using a nanoparticle size and zeta potential analyzer (Malvern Panalytical, UK). Antibodies against CLDN1, PDPN, Arg1, and Slamf7 were purchased from ABclonal Biotechnology (Wuhan, China). Antibodies against TGF-β1, Collagen I, α-SMA, TNF-α, Adgre1, iNOS, FN1, and IL-1β were purchased from Bioss Biotechnology (Beijing, China). Anti-FOXJ1 antibodies were purchased from BOSTER Biotechnology (Wuhan, China). Anti-GSDMD antibodies were purchased from Wanlei Biotechnology (Shenyang, China). An anti-occludin (OCLN) antibody was purchased from Proteintech (Rosemont, USA).

Animals and treatment

Specific pathogen-free C57BL/6 mice (male, 8–10 weeks old) were purchased from Changsheng Biotechnology (Shenyang, China). Mice were housed under standard conditions (12 h light/12 h dark cycle, 22 ± 2 °C, 55 ± 5%) with food and water provided ad libitum. All animal procedures were performed in accordance with institutional guidelines and approved by the Ethical Committee for Animal Experiments of Northeast Agricultural University (Grant Number: 202305001). The mice were randomly assigned to two groups ($n = 15$ for each group), in terms of time, it is divided into 7 days group and 14 days group (Fig. S1). MWCNTs were sterilized and suspended in sterile phosphate-buffered saline (PBS) containing 0.1% F-68. The mixture was sonicated using a Scientz-IID ultrasonic homogenizer (Ningbo Scientz Biotechnology Co., Ltd., Ningbo, China) to achieve a homogeneous suspension. The mice were anesthetized with isoflurane. For the MWCNT-exposed group, each mouse received 40 μg of MWCNTs suspension (50 μL) via oropharyngeal aspiration. Control mice received an equal volume of vehicle (PBS with 0.1% F-68). At 7 or 14 days post-exposure, mice were humanely euthanized. Blood was collected via cardiac puncture to isolate serum, and fecal pellets were harvested from the rectum. Lung and intestinal (rectum) tissues were excised for downstream analyses. Portions of each tissue were fixed in formalin for histology or snap-frozen in liquid nitrogen for RNA extraction and other assays.

Histological and Immunofluorescence staining

Histopathological analysis was carried out essentially as described in former studies [28, 29]. Lung or rectum tissues were fixed, dehydrated, embedded, cut into 4 μm paraffin sections and mounted on glass slides. Histological slides were sequentially processed with hematoxylin and eosin (H&E), Masson's trichrome, and Sirius Red stains, and the resulting micro-architecture was imaged on a Zeiss Primo Star light microscope (Zeiss, Germany) or an Olympus polarizing microscope (Japan). For immunofluorescence, tissue sections were processed to detect specific protein markers. For antigen retrieval, slides were

heated in 10 mM citrate buffer (pH 6.0) or EDTA solution (pH 9.0) at 95 °C for 20 min and then cooled to room temperature. Sections were blocked with 5% goat serum in PBS for 1 h to prevent nonspecific binding. The target proteins were labeled using the nine-color fluorescence kit (Huilan Biological Technology, China) based on the tyramide signal amplification technology. Primary antibodies against target proteins of interest were applied to the sections and incubated overnight at 4 °C in a humidified chamber. After washing with PBS, slides were incubated with appropriate secondary antibodies (RCA054, Huilan Biological Technology, China) for 1 h at room temperature in the dark. Nuclei were counterstained with DAPI for 10 min, and slides were mounted with antifade mounting medium (Jiancheng Bioengineering Institute, China). In the cellular immunofluorescence experiment, antibody elution was carried out using the immunostaining antibody eluent (Servicebio Technology, China), and other steps were conducted as described in the preceding immunofluorescence protocol. The Arg1 antibody was used at a 1:4000 dilution, while all other antibodies were diluted 1:500. The sections were imaged using an Fv3000 confocal microscope system (Olympus, Japan). Co-localization analysis was performed using ImageJ Fiji software by quantifying the overlap between the corresponding fluorescence channels within regions of interest.

Ultrastructural analysis

Lung specimens were diced into ≤ 1 mm^3 fragments and immediately fixed in 2.5% glutaraldehyde at 4 °C overnight. The samples were then processed to prepare ultrathin sections according to standard protocols [30]. Following routine processing, ultrathin sections were prepared and examined with a Hitachi H-7650 transmission electron microscope (TEM; Hitachi, Japan).

10× visium Spatial transcriptome sequencing

Spatial transcriptome sequencing using the 10x Visium V2 platform was performed on paraffin-embedded lung tissue sections from control and MWCNTs-treated mice (sampled on day 14 of the experimental period). The analysis was conducted by Shanghai OE Biotech Co., Ltd. (Shanghai, China).

mRNA sequencing

RNA sequencing in lung tissues from Control and MWCNTs-treated mice (sampled on day 14 of the experimental period) was performed by E-Gene Biotechnology Co., Ltd. (Shenzhen, China). The details are basically carried out in the same way as previous studies [31].

Quantitative real-time PCR

Tissue or cell samples were cryogenically homogenized with a SCIENTZ-48 L high-flux grinder (Ningbo Scientz Biotechnology, China). Total RNA was isolated using TRIzol reagent, and RT-qPCR was conducted according to a previously published protocol [32, 33]. with gene-specific primers listed in Table S1 (synthesized by Sangon Biotech, Shanghai, China). Transcript abundance was normalized to the reference gene and expressed using the $2^{-\Delta\Delta Ct}$ method.

16S rRNA gene sequencing

Library construction and Illumina sequencing were performed by E-Gene Biotechnology Co., Ltd. (Shenzhen, China). Briefly, total DNA was extracted from the stool samples using the QIAamp DNA stool extraction kit (Qiagen, Germany). The genomic DNA was examined by 1% agarose gel electrophoresis. All samples were quantified on a Qubit 2.0 Fluorometer (Thermo Fisher Scientific, USA).

Serum and fecal metabolomic profiling

Metabolite detection was performed at E-Gene Biotechnology Co., Ltd. (Shenzhen, China) using the method described previously [28].

Cell culture

MH-S cells (Procell Life Science & Technology Co., Ltd., Wuhan) were cultured in RPMI-1640 (MA0215, Meilun) medium supplemented with 10% FBS (AB-FBS0500, ABW) and 1% penicillin/streptomycin (P1400, Solarbi) under standard conditions (37 °C, 5% CO_2). Unless otherwise specified, for MWCNTs stimulation experiments, cells were exposed to MWCNTs at a concentration of 80 μg/mL for 24 h, after which cells or conditioned media were harvested. For MWCNTs under submerged conditions, agglomeration and sedimentation mean that nominal concentrations may not equal the delivered cellular dose, which can represent only a fraction of the administered dose [34].

Cell viability assay

In the cytotoxicity and proliferation assay, MH-S cells were treated with MWCNTs at a gradient of concentrations (0, 50, 100, 150, 200, 250, 300, 350, 400, 500, 600, and 700 μg/mL) to evaluate dose-dependent effects. After treatment, 10 μL CCK-8 kit (Beyotime Biotechnology, China) reagent was added to each well and incubated for 4 h. Finally, the plate reader (Molecular Devices, Shanghai, China) was used to measure the solution's absorbance values at 450/630 nm. The optical density was represented the relative value of cell viability. Cell viability was assessed using the Calcein-AM/PI Cell Viability/Cytotoxicity Assay Kit (Beyotime Biotechnology, China). After experimental treatments, cells were gently washed with PBS and incubated with Calcein-AM/PI working solution at 37 °C for 30 min in the dark. Fluorescence

images were captured using a fluorescence microscope (Leica DMi8, Germany). Accordingly, 80 μg/mL (approximately 25% of the IC_{50}) was used as the working concentration in the *in vitro* mechanistic assays to minimize confounding from overt cytotoxicity.

γ-H2AX Immunofluorescence assay

DNA double-strand-break formation was assessed with the DNA Damage Assay Kit (Beyotime Biotechnology, China). Paraffin-embedded lung slices (3 μm) were dewaxed in xylene, re-hydrated through graded ethanol, and rinsed in PBS. MH-S cells were collected by centrifugation and then fixed with the fixative in the kit for 15 min. Cells or tissues were labelled sequentially with the γ-H2AX primary antibody (1 h, 25 °C) and FITC-conjugated secondary antibody (1 h). DAPI counter-staining and mounting were performed as described above. Fluorescence images were captured on a Fv3000 confocal microscope system (Olympus, Japan).

RNA oligonucleotide transfection

Cells were seeded in 6-well plates (1×10^6 cells/well) 24 h prior to reach 60–70% confluence. siRNAs against Slamf7 (sense: 5′-UAAGUGGAGGGCACAAGUCG T-3′; antisense: 5′-CGACUUGUGCCCUCACUUAT-3′) and scrambled negative control (NC) siRNA (Sangon Biotech, China) were complexed with RNATransMate (Sangon Biotech, China). Following 15 min incubation at room temperature, complexes were added to cells.

Cytokine and oxidative stress assays

The concentrations of TNF-α and IL-1β in mouse serum and macrophage culture supernatants were measured using ELISA kits (Biorbyt, Britain) following the manufacturer's instructions. Malondialdehyde (MDA) and reactive oxygen species (ROS) were quantified using assay kits (Jiancheng Bioengineering Institute, China) following the manufacturer's instructions. The details are basically carried out in the same way as previous studies [35].

PPI analysis

Protein–protein interaction (PPI) analysis of relatively expressed genes was carried out according to the STRING database (version: 11.5, website link: https://cn.string-db.org/). We input the gene in the list and selected Mus musculus as the organism. We constructed networks for the species from the database according to the selected target gene.

Statistical analyses

Data are presented as mean ± SEM, unless otherwise specified. For comparisons between two groups, an unpaired two-tailed Student's t-test was used. For comparisons among multiple groups, one-way analysis of variance (ANOVA) followed by Tukey's post hoc test was applied. $p < 0.05$ was considered statistically significant. Differential gene expression analysis was conducted using the DESeq2 package in R. Metabolomic and microbiome data were analyzed using multivariate statistical approaches including principal component analysis (PCA), partial least squares discriminant analysis (PLS-DA), and linear discriminant analysis effect size (LEfSe). Correlation analyses were performed using Pearson's correlation coefficient.

Results

MWCNT exposure promotes lung inflammation and fibrosis in mice

Observation with scanning electron microscope verified the characteristic hollow, tubular morphology of the MWCNTs (Fig. 1A). Dynamic light scattering (DLS) showed an intensity-weighted Z-average hydrodynamic diameter of 316.6 ± 25.4 nm with a polydispersity index (PDI) of 0.365 ± 0.029 (Fig. S2A and B). Electrophoretic light scattering revealed a negative zeta potential of − 30.74 ± 1.18 mV (Fig. S2C). The specific test method is illustrated in Fig. 1B. H&E histology revealed marked pulmonary lesions in MWCNT-exposed mice, evidenced by vascular congestion, thickened alveolar septa, and dense inflammatory infiltrates within alveolar spaces and around blood vessels (Fig. 1C). Masson's trichrome staining further indicated extensive collagen deposition in the lung tissues of MWCNT-exposed mice (Fig. 1D). Sirius Red histochemistry revealed pronounced lung fibrosis in MWCNT-treated mice, highlighted by substantial deposition of collagen type I (red) and type III (green) (Fig. 1E). Quantitative analysis of Sirius Red-stained sections revealed a more than three-fold increase in collagen-positive areas of the lungs after 14 days of MWCNT exposure compared to controls (Fig. 1F). These results showed that 14 days after MWCNT exposure, mouse lungs exhibited significant inflammatory cell infiltration and fibrosis.

MWCNT exposure markedly up-regulates pro-inflammatory signaling in mouse lungs

To bulk mRNA-sequencing and spatial transcriptomics convergently demonstrate that MWCNTs trigger a striking immune-driven reprogramming of lung tissue 14 days after exposure. In bulk RNA-seq, 2454 differentially expressed genes (DEGs) ($|\log_2 FC| \geq 1$, adjusted p-value ≤ 0.05) were detected, with a predominance of up-regulation (1669 genes). Among the top ten DEGs, the expression levels of *Cd68*, *Saa3*, and *Gpnmb* were significantly upregulated (Fig. 2A). Cd68 and Mpeg1 are recognized as marker genes for macrophages [36, 37], while Saa3, Gpnmb, and Cybb are commonly linked to inflammatory

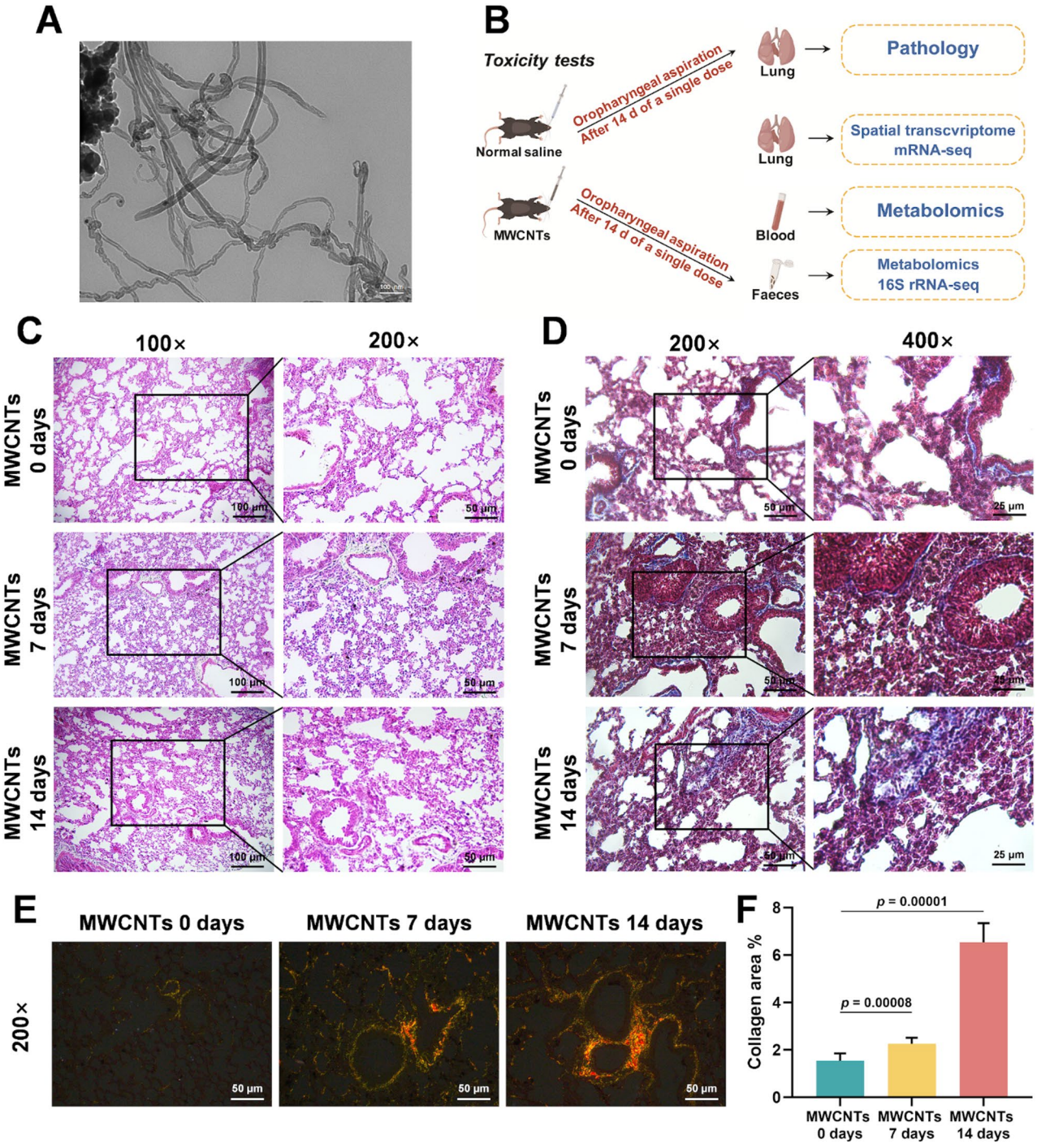

Fig. 1 MWCNT-induced pathological changes in mouse lung tissues. (**A**) Scanning electron microscope image showing the tubular structure of MWCNTs. (**B**) Test process. H&E (**C**), Masson (**D**) and Sirius Red staining (**E**) of mouse lungs. (**F**) Collagen-positive regions identified by Sirius Red staining were quantified and reported as mean ± SEM ($n = 5$)

responses and oxidative stress [38–40]. These findings indicate that exposure to MWCNT activates the immune system, leading to inflammation and oxidative stress in the lungs. Additionally, the downregulation of *Adamts5* may contribute to impaired extracellular matrix degradation, thereby promoting fibrotic deposition. The downregulation of antioxidant genes *Sod3*, *Gpx3*, and *Gsta3* exacerbates oxidative stress (Fig. 2B). KEGG pathway enrichment analysis further revealed that the top five pathways were mainly associated with phagosome formation, cytokine receptor interactions, and other immune response-related pathways (Fig. 2C). These results

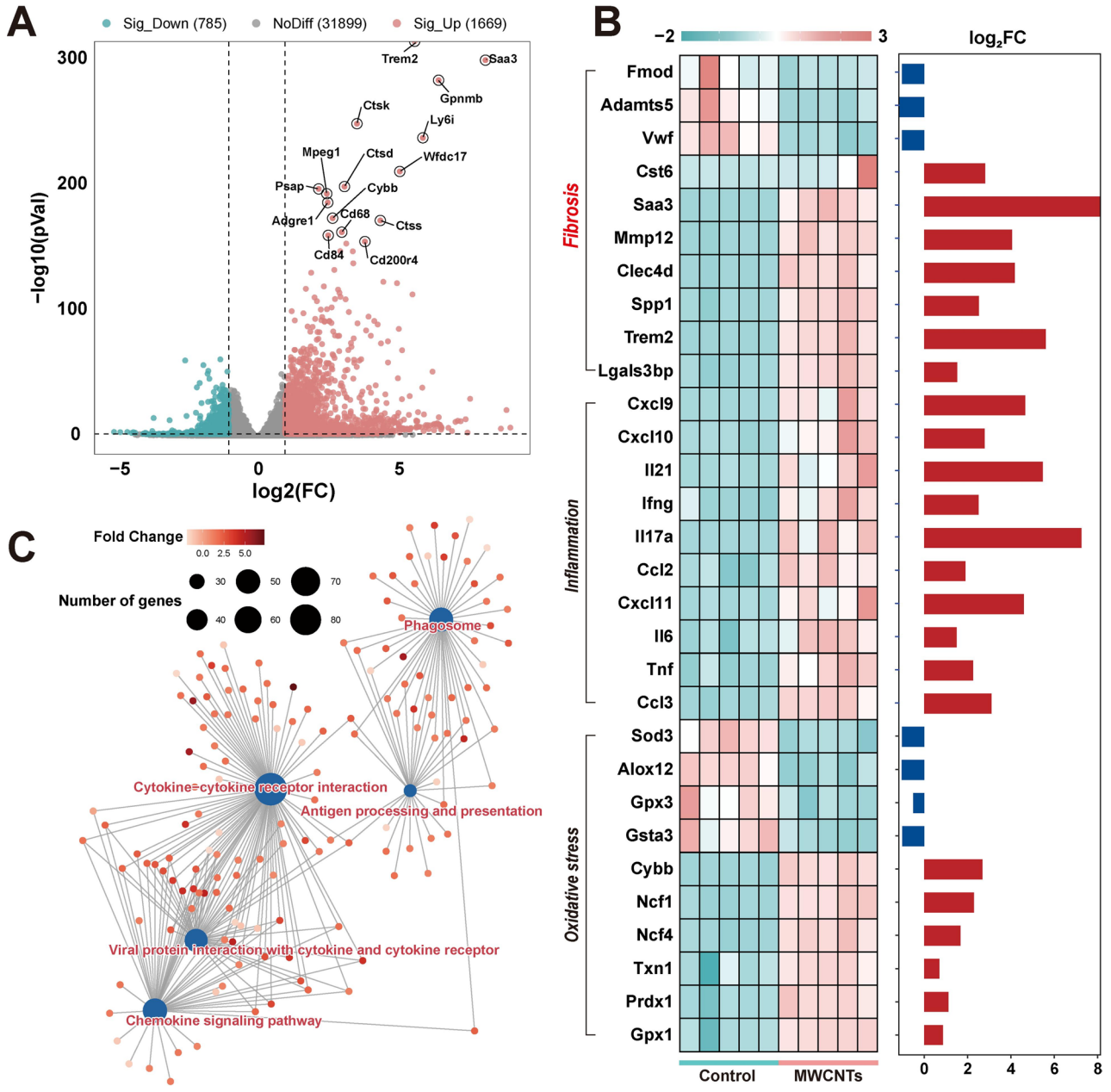

Fig. 2 Transcriptomic changes in mouse lungs following exposure to MWCNTs ($n = 5$). (**A**) Volcano plot depicting DEGs. (**B**) Changes in genes associated with lung inflammation and fibrosis after exposure to MWCNTs. (**C**) KEGG pathway enrichment analysis highlighting the five most significant pathways dysregulated by MWCNT exposure

provide a foundation for further investigation into the molecular mechanisms underlying MWCNT-induced lung fibrosis.

Comparative analysis of cellular composition and gene expression in mouse lungs following MWCNT exposure

Understanding where each cell sits in the tissue is key to deciphering cell-to-cell communication in both normal and diseased lungs. Standard methods like immunohistochemistry or fluorescence microscopy can show single proteins, yet they visualize only a few markers at a time and require targets to be chosen beforehand. Therefore, we used the 10x Visium spatial RNA sequencing platform to generate high-throughput transcriptome capture from the lungs of control and MWCNTs group mice on day 14 after MWCNT exposure (Fig. 3A). Spatial transcriptomic data were analyzed to explore the spatial organization of the lung tissue. Unsupervised clustering of spots in all samples based on cell type composition identified nine clusters, which we defined as major cell type

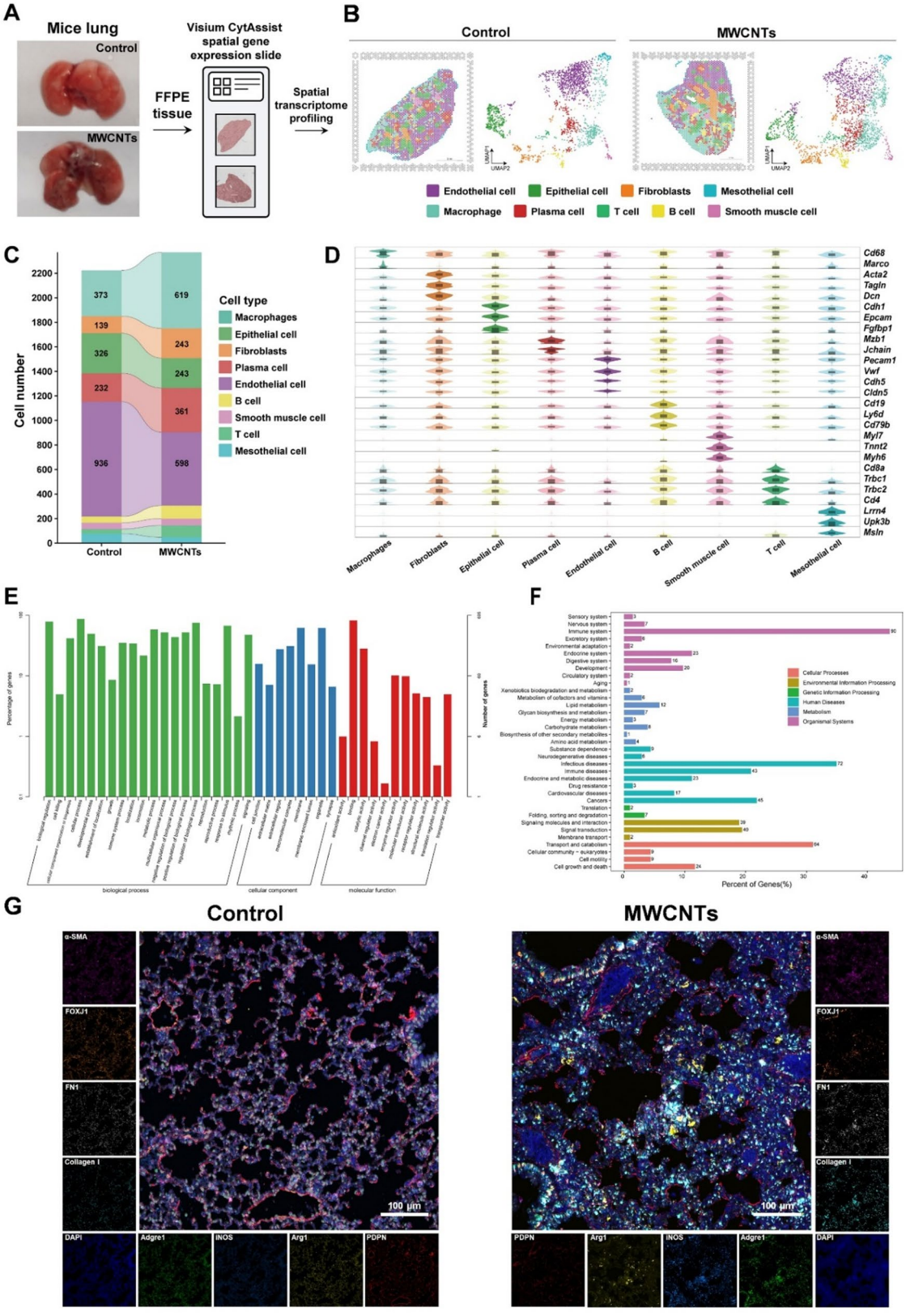

Fig. 3 Spatial transcriptomics of mouse lungs exposed to MWCNTs. (**A**) Spatial maps (10x Visium) showing cell-type distribution at day 14. (**B**, **C**) Unsupervised clustering into nine dominant niches annotated by marker genes. (**D**) Marker-gene expression across clusters. KEGG pathway (**E**) and GO (**F**) enrichment analysis of lung spatial transcriptome differential genes. (**G**) Immunofluorescence staining of representative cell markers in MWCNT-exposed mouse lungs

niches. Using established marker genes, we annotated each cluster to a dominant cell type (Fig. 3B), including macrophages, fibroblasts, epithelial cells, plasma cells, endothelial cells, B cells, vascular smooth muscle cells, T cells and mesothelial cells. Because the Visium platform captures transcriptomes at ~55 μm per spot—coarser than single-cell scale—each spot inevitably contains transcripts from more than one cell. Consequently, spatial clusters show minor expression of markers from adjacent cell populations in addition to their defining signature genes. For instance, the fibroblast-dominated cluster most strongly expressed *Dcn*, yet many capture spots within this cluster also showed expression of *Lrrn4*, a gene associated with mesothelial cells. After exposure to MWCNTs, the area dominated by macrophages in the mouse lungs increased to 1.66-fold that of the control group, while the area dominated by fibroblasts increased to 1.75 times the original value (Fig. 3C). The distribution scores for each dominant cell type are presented in Fig. 3C, and the corresponding marker gene expression levels across clusters are shown in Fig. 3D. Furthermore, KEGG and GO enrichment analysis of DEGs within the spatial transcriptome showed that immune response, energy metabolism, signal receptor binding and other pathways were significantly affected by MWCNTs (Fig. 3E and F). Additionally, immunofluorescence staining was performed to identify representative markers of key cell types in the lung, including α-SMA (vascular area), FOXJ1 (bronchiolar area), FN1 (fibroblast area), Collagen I (myofibroblast area), Adgre1 (macrophage area), iNOS (M1 macrophage area), Arg1 (M2 macrophage area), and PDPN (alveolar area) (Fig. 3G). The results showed a significant increase in macrophages, particularly M1-type macrophages, in MWCNT-exposed lung tissue. Collagen I expression was elevated and coincided with the FN1 expression region, suggesting that MWCNTs promotes the differentiation of fibroblasts into myofibroblasts, contributing to fibrosis progression. These findings provide critical spatial insights into the cellular remodeling and molecular dysregulation underlying MWCNT-induced lung fibrosis.

Respiratory burst of macrophages in mice lung exposed to MWCNTs

Transcriptome analysis of lung tissue revealed that Cybb, a critical subunit of the NADPH oxidase 2 (NOX2) complex, was among the top 15 DEGs. NOX2 is responsible for transferring electrons from cytoplasmic NADPH across the phagosomal membrane to molecular oxygen, reducing it to superoxide anion [41]. This process leads to a rapid increase in oxygen consumption and initiates "respiratory burst" [42]. The high levels of ROS generated during the respiratory burst can cause extensive oxidative damage to cellular components, including DNA. Among the various forms of oxidative DNA damage—such as base modifications, abasic sites, DNA-protein crosslinks, and strand breaks—double-strand breaks are considered the most severe [43]. Consistent with these findings, we observed a significant upregulation of the NADPH oxidase complex in alveolar macrophages from MWCNT-exposed mice, as shown in Fig. 4A. To further investigate the molecular basis of macrophage activation, we conducted PPI network analysis of key components of the NADPH oxidase complex, including Cyba, Cybb, Noxa1, Ncf1, Ncf2 and Ncf4. The PPI analysis revealed strong interactions among these proteins, suggesting a coordinated upregulation of the NOX2 complex following MWCNT exposure (Fig. 4B). Consistently, heatmap analysis of transcriptomic data showed that the expression levels of these six genes were significantly elevated in the lungs of MWCNT-exposed mice compared to controls (Fig. 4C). Given the substantial ROS production induced by respiratory bursts, we next examined oxidative DNA damage. Immunofluorescence staining for γ-H2AX, a marker of DNA double-strand breaks, revealed a marked increase in γ-H2AX-positive signals in the lung tissues of MWCNT-exposed mice relative to controls (Fig. 4D), indicating the occurrence of severe DNA damage. When DNA double-strand breaks occur, γ-H2AX is rapidly and extensively phosphorylated, which serves as a marker of DNA damage [44]. The broken DNA double-strands are sensed by Aim2, which then triggers the Aim2 inflammasome pathway, leading to the activation of Casp1 and the induction of pyroptosis (Fig. S3). TEM of lung tissues provided ultrastructural evidence of cell death. In MWCNT-exposed lungs, macrophages exhibited hallmark features of pyroptosis, including chromatin condensation (green arrows), endoplasmic reticulum swelling (red arrows), and plasma membrane rupture (yellow arrows) (Fig. 4E). Spatial transcriptomic analysis further demonstrated that pyroptosis-associated gene signatures were highly enriched in areas dominated by macrophages within the lung tissue (Fig. 4F). Notably, regions with high pyroptotic gene expression overlapped substantially with macrophage-enriched zones, suggesting that macrophages are a primary cell type undergoing pyroptosis in response to MWCNT exposure.

Slamf7–Slamf7 promotes superactivation of macrophages following MWCNT exposure

Given the prominent inflammatory activation of macrophages observed after MWCNT exposure, we next investigated potential intercellular communication events driving this process. Macrophages were further classified into M1 type macrophages and M2 type macrophages (Fig. S4). Cell–cell communication analysis revealed that the Slamf7–Slamf7 interaction pair exhibited the highest number of interaction events among all ligand–receptor

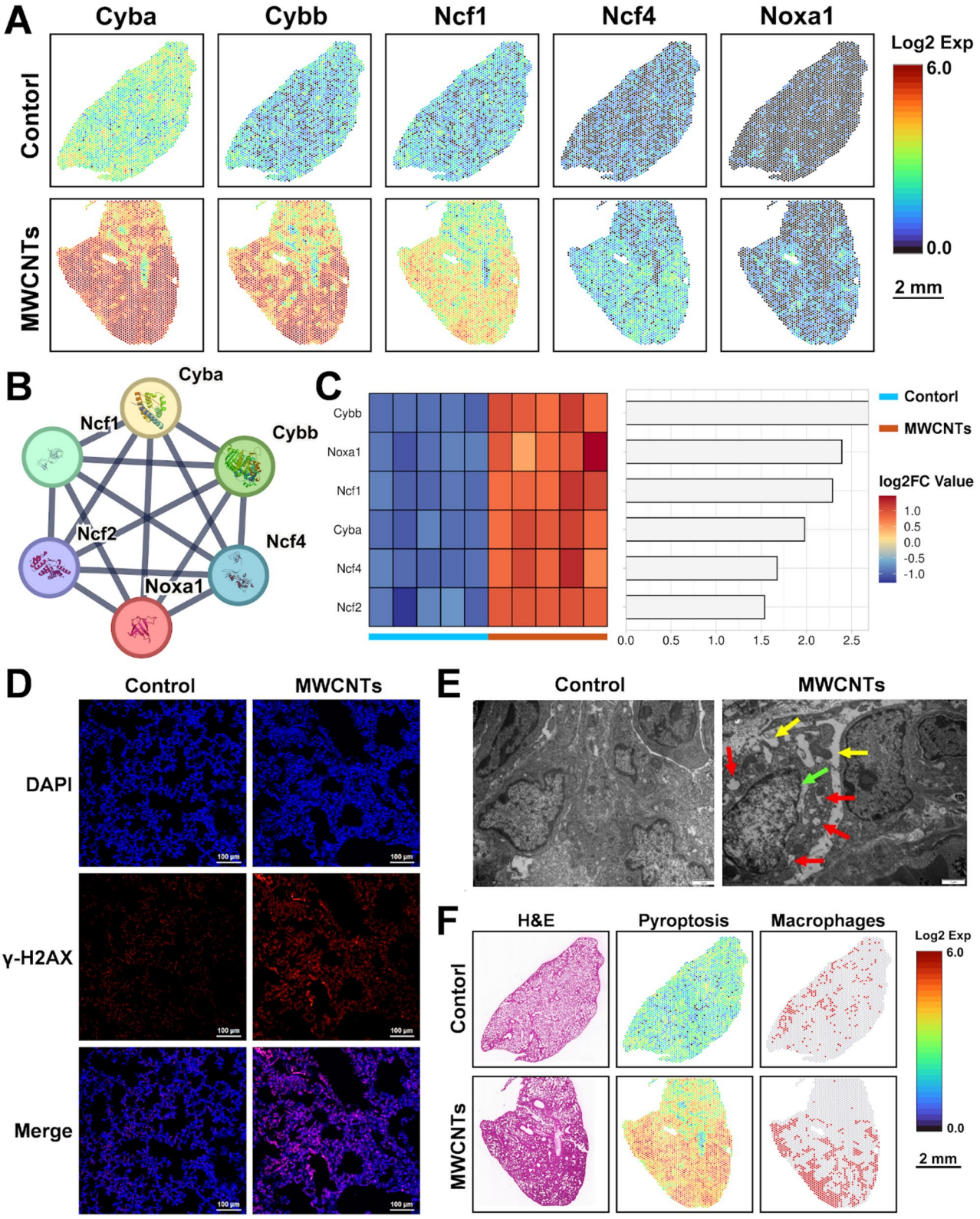

Fig. 4 Respiratory burst, DNA damage, and pyroptosis in mouse lungs following MWCNT exposure. (**A**) Expression levels of NADPH oxidase complex components (*Cyba*, *Cybb*, *Ncf1*, *Ncf2*, *Noxa1*, and *Ncf4*) in alveolar macrophages. (**B**) PPI network analysis showing interactions among NADPH oxidase complex genes. (**C**) Heatmap of differentially expressed NADPH oxidase-related genes from bulk RNA sequencing. (**D**) Immunofluorescence staining for γ-H2AX in lung tissues, demonstrating increased DNA double-strand breaks after MWCNT exposure. (**E**) TEM images, including chromatin condensation (green arrows), endoplasmic reticulum swelling (red arrows), and plasma membrane rupture (yellow arrows). (**F**) Spatial distribution of pyroptosis-related gene signatures and macrophage-enriched regions in lung tissue sections based on spatial transcriptomics

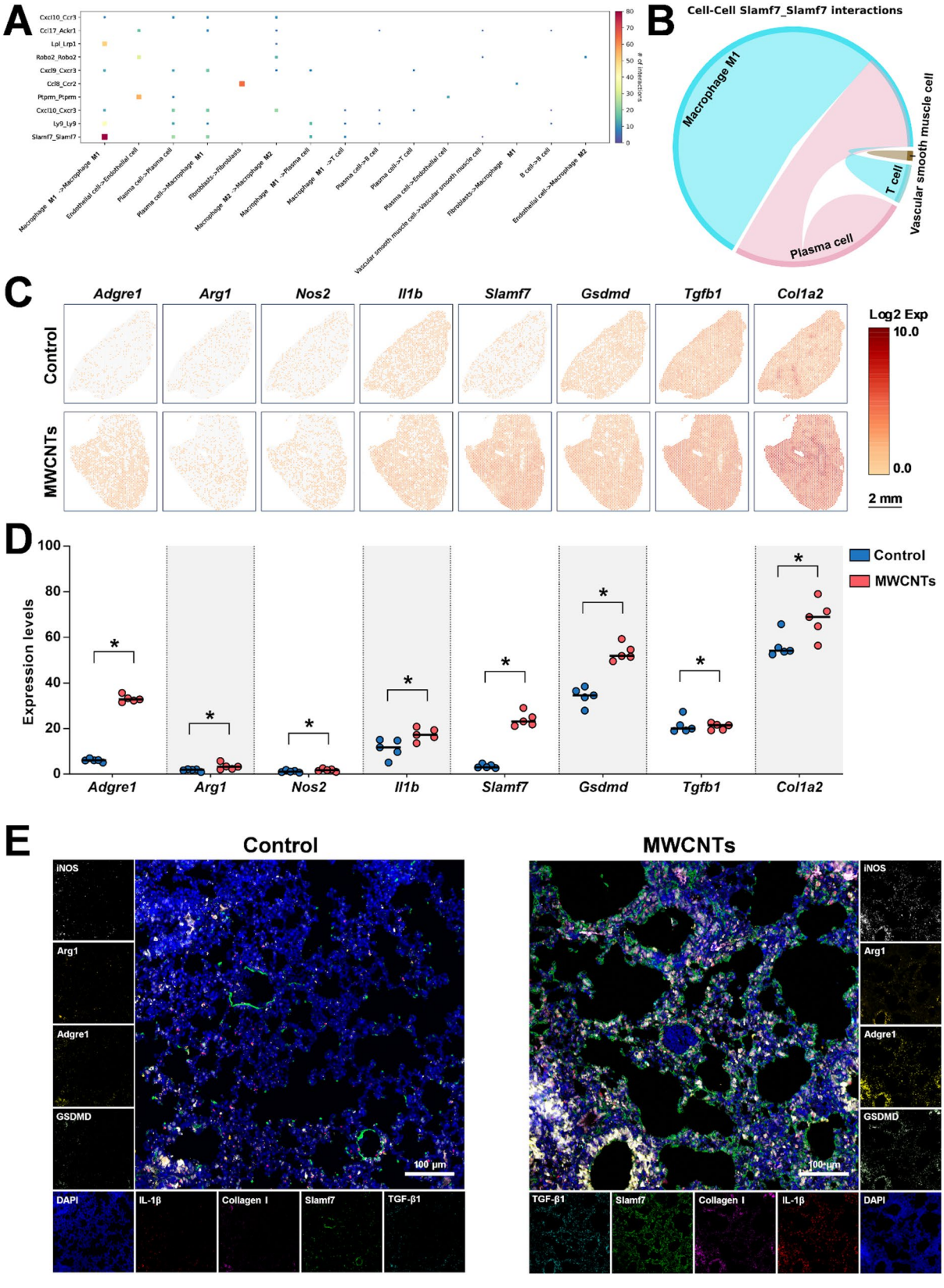

Fig. 5 (See legend on next page.)

(See figure on previous page.)

Fig. 5 Slamf7-Slamf7 interaction mediates macrophage superactivation following MWCNT exposure. (**A**) Cell–cell communication analysis based on spatial transcriptomics of MWCNT-exposed lung tissue. (**B**) Interaction network showing cell type-specific interactions involving the Slamf7-Slamf7 ligand–receptor pair. (**C**) Spatial transcriptomic expression maps of *Slamf7*, *Nos2*, *Tgfb1*, *Col1a2*, *Arg1*, *Il1b*, *Gsdmd*, and *Adgre1* in lung sections from Control and MWCNT-exposed mice. (**D**) RNA-seq analysis showing consistent upregulation of these genes in MWCNT-exposed lungs. (**E**) Immunofluorescence staining of corresponding proteins in mouse lung tissues. A *p* value of less than 0.05 is considered significant (significance is denoted as *)

pairs in MWCNT-exposed lungs (Fig. 5A). Further analysis of Slamf7–Slamf7-specific interactions demonstrated that this signaling axis was predominantly active between macrophages (Fig. 5B), suggesting that Slamf7–Slamf7 signaling between macrophages may establish an autocrine/paracrine amplification loop that reinforces inflammatory superactivation. To validate these findings, we assessed the spatial expression patterns of key inflammatory and fibrotic markers. Spatial transcriptomics data showed significantly increased expression of *Slamf7*, *Nos2*, *Tgfb1*, *Col1a2*, *Arg1*, *Il1b*, *Gsdmd*, and *Adgre1* in MWCNT-exposed lung tissues compared to controls (Fig. 5C). These trends were consistent with the results from bulk RNA sequencing (Fig. 5D). Immunofluorescence staining further confirmed the localization of Slamf7 within areas enriched for M1-polarized macrophages, as indicated by strong co-expression with iNOS and Adgre1 (Fig. 5E, Fig. S5). These regions also exhibited elevated levels of pro-inflammatory factors, consistent with an activated macrophage phenotype. The activation state of macrophages is tightly regulated by environmental signals and receptor-mediated pathways [45, 46], with cytokines playing a major role in enhancing macrophage responsiveness. Previous studies have shown that Slamf7 upregulation is associated with heightened macrophage activation in inflammatory diseases such as inflammatory bowel disease and COVID-19 pneumonia [47]. Slamf7 engagement has been demonstrated to superactivate macrophages, driving robust inflammatory responses [47, 48]. Therefore, targeting Slamf7 or its downstream pathways may help mitigate macrophage-driven inflammation and fibrosis caused by MWCNTs. Notably, this pro-inflammatory activation is not necessarily detrimental. In cancer therapy, where MWCNTs are also explored as drug carriers, Slamf7-mediated macrophage superactivation may enhance anti-tumor immunity by promoting M1 polarization.

Validation of Slamf7-mediated pro-inflammatory superactivation in MWCNT-exposed macrophages in vitro

To further investigate the role of Slamf7 in MWCNT-induced macrophage activation, we conducted a series of in vitro experiments using MH-S mouse alveolar macrophages. First, a cell viability assay was performed across a wide range of MWCNTs concentration (0–700 μg/mL) to assess cytotoxicity. A dose-dependent decrease in cell viability was observed, and the calculated IC50 value was 353.5 μg/mL (Fig. 6A). Based on these results, a sub-cytotoxic concentration of 80 μg/mL was selected for subsequent mechanistic studies. Upon exposure to MWCNTs, microscopic examination revealed progressive uptake of MWCNTs by macrophages over time, indicated by accumulation of visible black granules in the cytoplasm (Fig. 6B). DNA damage in macrophages was confirmed by γ-H2AX immunofluorescence staining, which showed a significant increase in γ-H2AX-positive nuclei after MWCNTs treatment, suggesting the occurrence of DNA double-strand breaks (Fig. 6C). In addition, the number of dead cells increased after MWCNT exposure (Fig. S6). To assess macrophage polarization and activation status, we performed immunofluorescence staining for iNOS and Arg1, markers of M1 and M2 polarization, respectively. MWCNT exposure led to increased iNOS expression with minimal changes in Arg1, indicating M1-type polarization. Notably, surface expression of Slamf7 and GSDMD was also enhanced in MWCNT-treated cells, suggesting membrane pore formation and pyroptotic potential (Fig. 6D). Additionally, elevated expression of Slamf7, TNF-α, and IL-1β was detected in MWCNTs-treated macrophages (Fig. 6E). To directly examine the role of Slamf7 in inflammatory signaling, we silenced its expression using siRNA. Knockdown efficiency was validated at the gene level, showing a substantial reduction of Slamf7 expression in MWCNT-treated macrophages transfected with si-Slamf7 (Fig. 6F). Furthermore, *Tnf* mRNA levels were significantly reduced in the si-Slamf7 group compared to the non-silencing control following MWCNT exposure (Fig. 6G). Consistently, ELISA analysis revealed that the secretion levels of TNF-α and IL-1β were markedly increased after MWCNTs treatment, while siRNA-mediated silencing of Slamf7 attenuated this pro-inflammatory response (Fig. 6H, I). Thus, MWCNTs not only induce direct DNA double-strand break and cytotoxic stress in macrophages, but also drive their polarization toward a pro-inflammatory M1 phenotype. The elevated expression of Slamf7 on the cell surface, along with increased levels of inflammatory cytokines such as TNF-α and IL-1β, underscores the critical role of Slamf7 in amplifying macrophage activation. Importantly, silencing Slamf7 effectively attenuated the inflammatory response, indicating that Slamf7 acts as a key regulator of macrophage-mediated inflammation following MWCNT exposure.

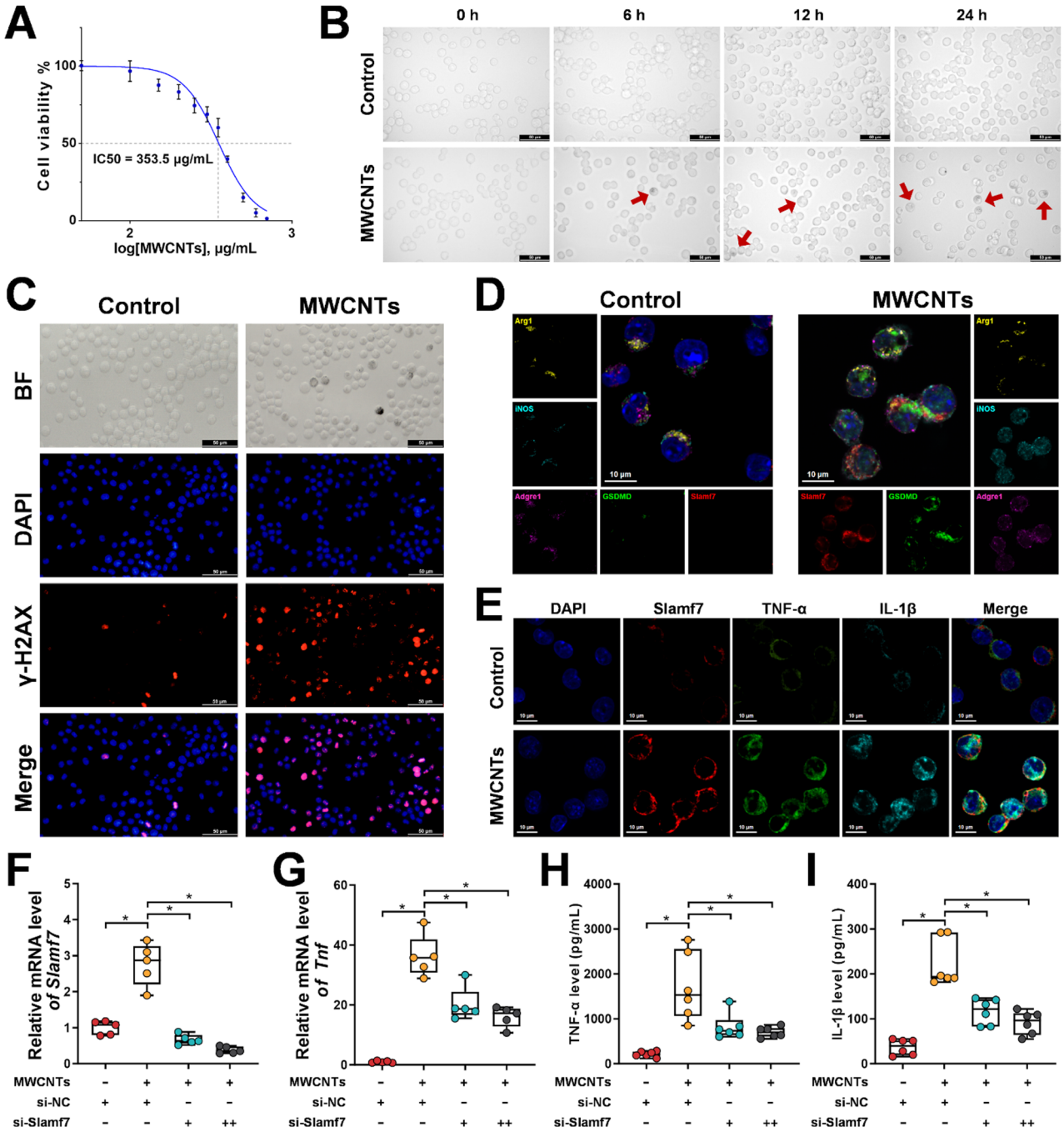

Fig. 6 In vitro validation of macrophage responses to MWCNTs. (**A**) Cell viability of MH-S cells after treatment with increasing concentrations of MWCNTs for 24 h. (**B**) Internalization of MWCNTs by MH-S cells over time observed under microscopy. (**C**) Immunofluorescence staining of γ-H2AX in MH-S cells after MWCNT exposure. (**D**) Immunofluorescence detection of macrophage polarization markers (Adgre1, iNOS, Arg1) and inflammatory-related proteins (Slamf7, GSDMD). (**E**) Immunofluorescence staining of Slamf7, TNF-α, and IL-1β in MH-S cells. (**F**) Validation of Slamf7 knockdown efficiency by siRNA in MWCNT-treated MH-S cells. (**G**) Relative mRNA level of *Tnf* in cells with or without Slamf7 knockdown. ELISA measurement of TNF-α (**H**) and IL-1β (**I**) levels in the supernatant of MWCNT-treated MH-S cells with or without Slamf7 knockdown. A *p* value of less than 0.05 is considered significant (significance is denoted as *)

Serum metabolomics revealed systemic metabolic dysregulation and spread of inflammation after MWCNT exposure

To investigate the systemic metabolic alterations induced by exposure to MWCNTs, we performed a comprehensive serum metabolic profiling. The principal component analysis (PCA) of serum metabolites from mice exposed to MWCNTs (Fig. 7A) revealed a distinct separation

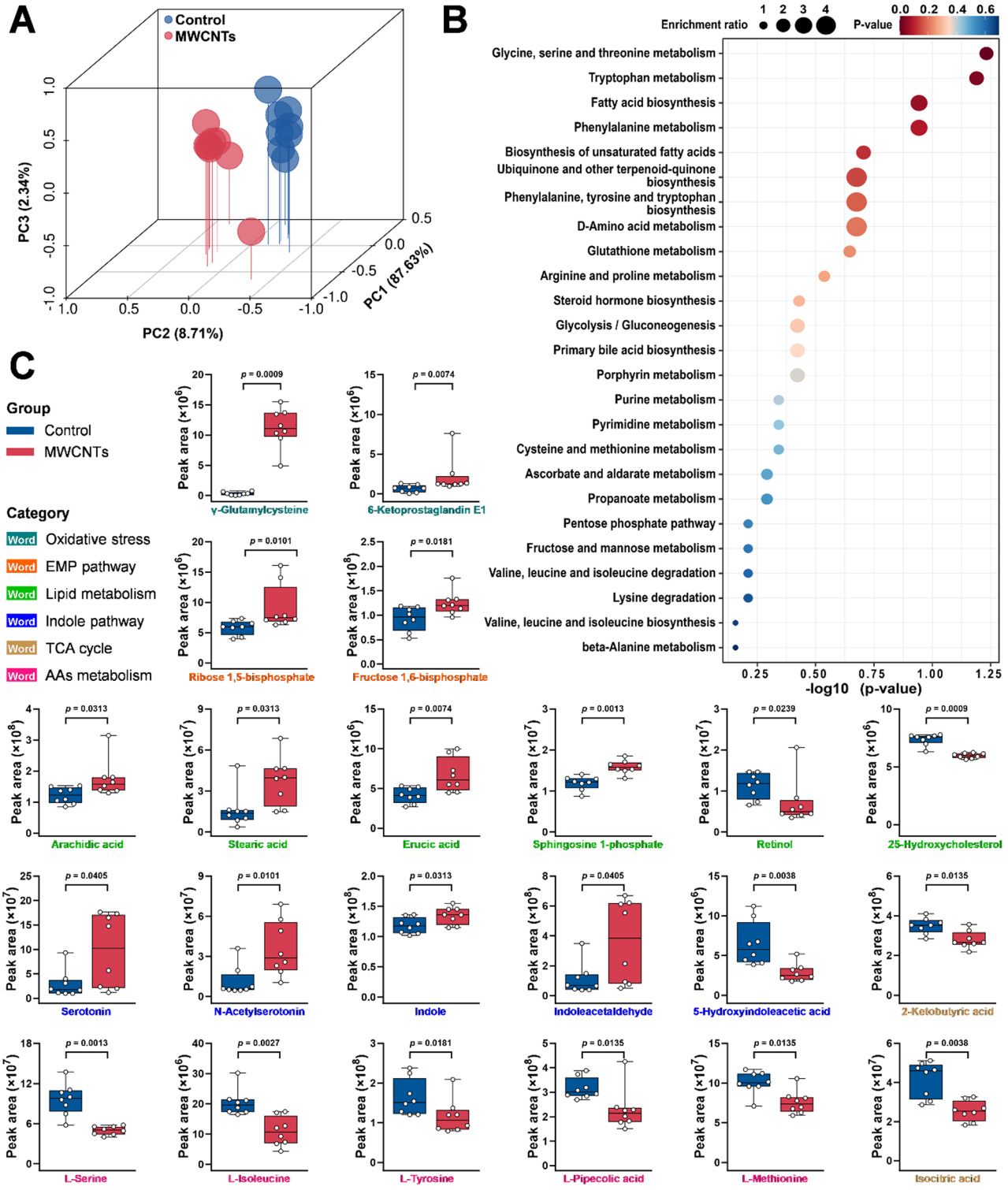

Fig. 7 Serum metabolomics analysis of mice after MWCNT exposure. (**A**) Principal component analysis (PCA) of serum metabolite profiles from control and MWCNT-exposed mice. (**B**) KEGG pathway enrichment analysis of significantly altered metabolites. (**C**) Relative abundance of representative differential metabolites involved in oxidative stress and energy metabolism pathways

between the control and MWCNTs groups, suggesting significant metabolic alterations induced by MWCNT exposure. A total of 76 metabolites with significant differences ($p < 0.05$, VIP > 1) were identified, of which 40 were upregulated and 36 were downregulated (Fig. S7A). KEGG pathway enrichment analysis of these differential metabolites (Fig. 7B) showed that they were primarily involved in amino acid metabolism and fatty acid metabolism pathways. Further analysis of metabolites with an $|\log_2 FC| > 1$ (Fig. S7B) supported these findings. Several metabolites associated with oxidative stress, including γ-glutamylcysteine, sphingosine-1-phosphate (S1P), and 6-ketoprostaglandin E1, were significantly elevated in the MWCNTs group. Notably, S1P, a bioactive lipid mediator, is known to activate inflammation-related signaling pathways and promote the release of pro-inflammatory cytokines, suggesting an enhanced systemic inflammatory state (Fig. 7C). In addition, metabolites related to glycolysis—such as fructose-1,6-bisphosphate and ribose-1,5-bisphosphate—were upregulated, whereas isocitric acid, a key intermediate of the tricarboxylic acid (TCA) cycle, was decreased. This metabolic shift may reflect increased energy demand driven by inflammation-induced cellular activation (Fig. 7C). Disruption of glycolytic and TCA cycle pathways could alter cellular energy metabolism, while aberrant lipid metabolism may contribute to the persistence of inflammation and progression of lung injury [49, 50]. Therefore, following MWCNT exposure, dysregulation of oxidative-stress–related metabolites in the bloodstream may exacerbate cellular and tissue damage.

Systemic inflammation and intestinal barrier disruption following MWCNT exposure

To further evaluate the systemic effects of MWCNT exposure, we assessed key inflammatory and oxidative stress markers in peripheral blood, as well as changes in the intestinal barrier. ELISA showed that the serum levels of pro-inflammatory cytokines TNF-α and IL-1β were markedly elevated, with an average increase of more than twofold in the MWCNT-exposed group compared to controls (Fig. 8A). In parallel, ROS and MDA levels in peripheral blood were significantly increased, indicating a systemic oxidative stress response (Fig. 8B). Considering the crosstalk between lung inflammation and gut homeostasis, we next evaluated the intestinal mucosa. Immunofluorescence staining of rectal tissues revealed increased expression of pro-inflammatory factors TGF-β1 and IL-1β, accompanied by a noticeable decrease in tight junction proteins OCLN and CLDN1 (Fig. 8C).

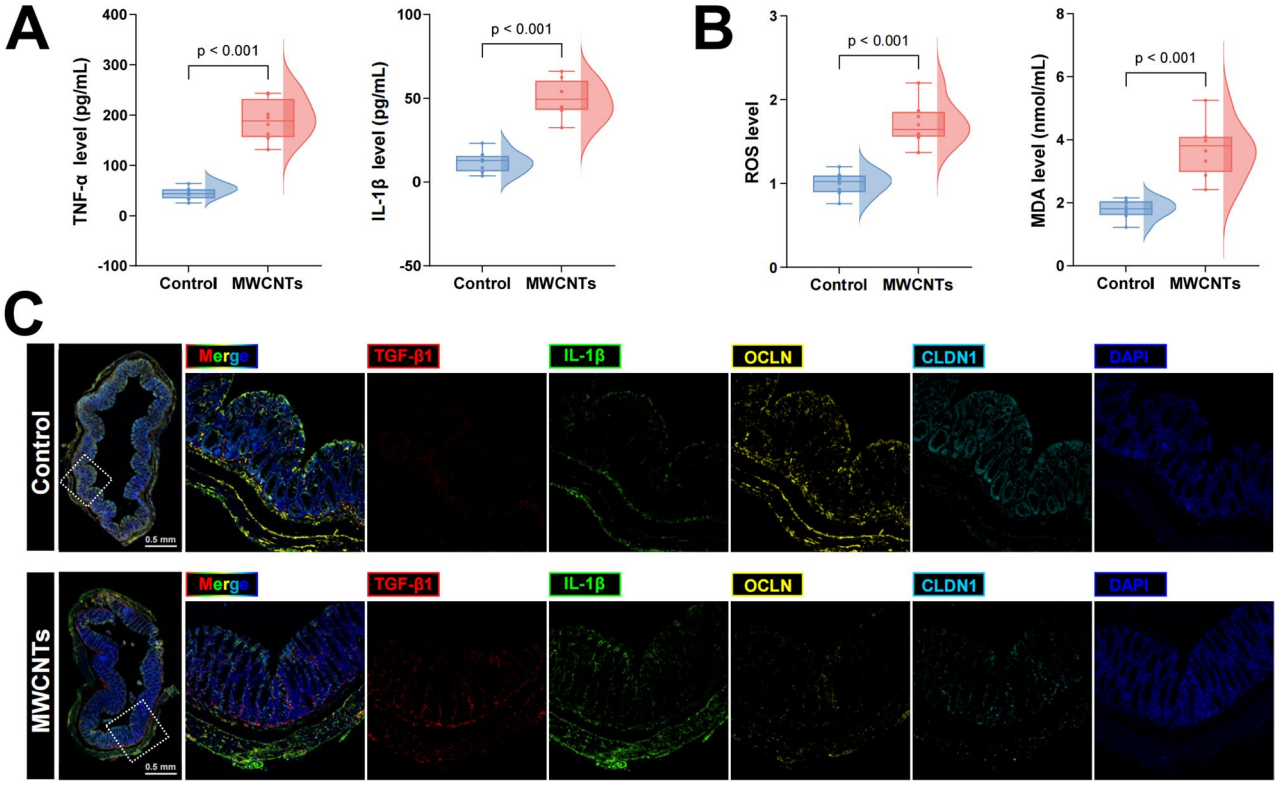

Fig. 8 Systemic inflammation and intestinal barrier impairment in mice after MWCNT exposure. (**A**) Serum levels of TNF-α and IL-1β in control and MWCNT-exposed mice (n = 7). (**B**) Relative levels of ROS and MDA in mouse serum. (**C**) Immunofluorescence staining of TGF-β1, IL-1β, OCLN, and CLDN1 in rectal tissue sections

These results suggest that MWCNT-induced pulmonary inflammation may extend beyond the lung, and is accompanied by systemic inflammatory responses and impairment of intestinal barrier integrity, potentially via circulating inflammatory/metabolic mediators, although direct gastrointestinal exposure after mucociliary clearance and swallowing cannot be excluded.

MWCNT exposure alters the composition of gut microbiota in mice

16S rRNA sequencing was performed on fecal samples collected from control and MWCNT-treated mice. Alpha diversity analysis using the Shannon and Simpson indices revealed no significant changes in microbial diversity between the two groups (Fig. 9A), suggesting that MWCNT exposure did not markedly affect overall microbial richness or evenness. However, non-metric multidimensional scaling (NMDS) analysis showed

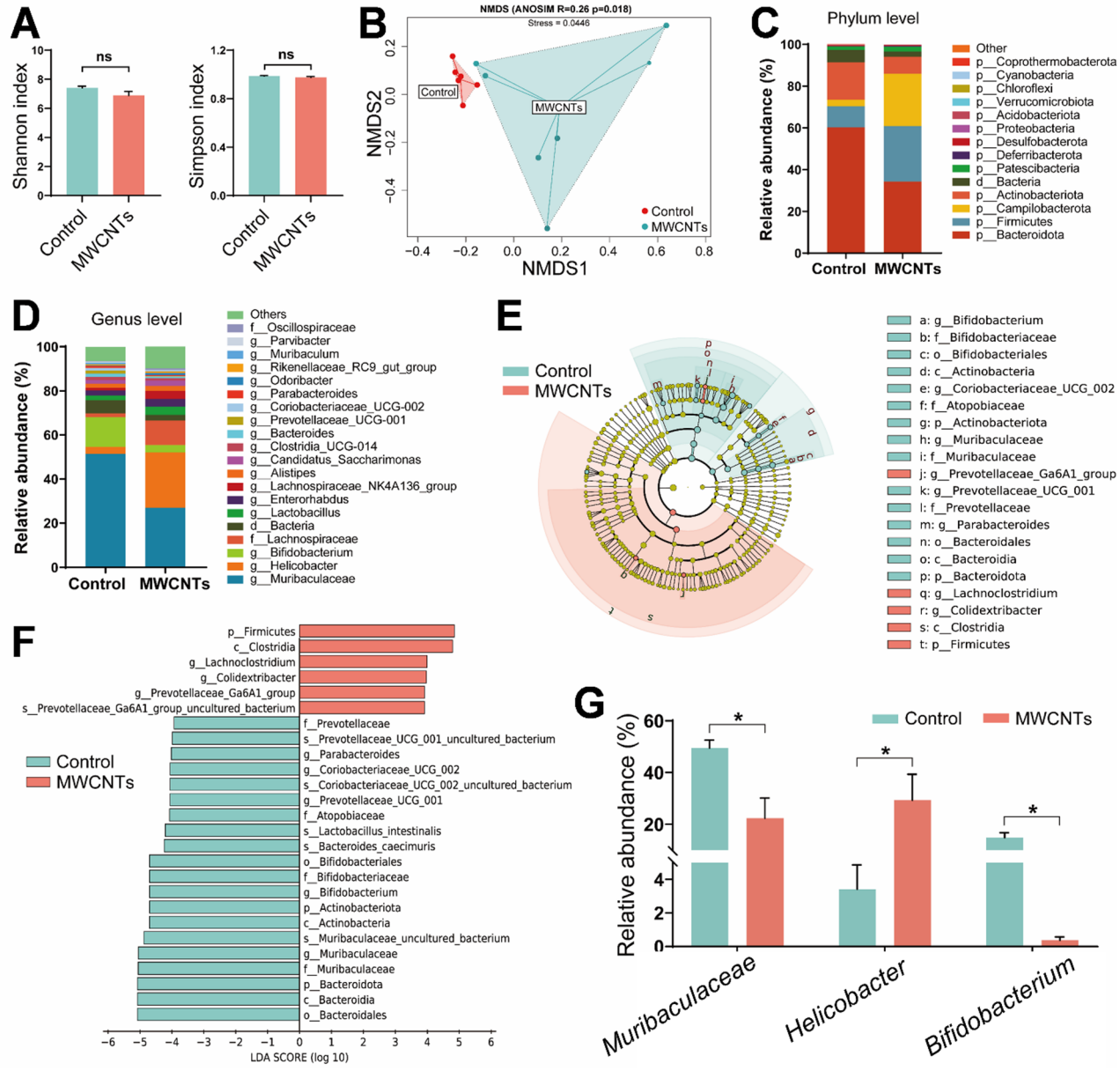

Fig. 9 Fecal microbiota composition analysis after MWCNT exposure. (**A**) Alpha diversity analysis using Shannon and Simpson indices. (**B**) NMDS plot based on Bray–Curtis distance showing distinct microbial community structures between the two groups. (**C**) Relative abundance of fecal microbiota at the phylum level. (**D**) Genus-level relative abundance showing changes in microbial composition. (**E**) Cladogram and (**F**) LDA score plot identifying taxa with differential abundance between groups. (**G**) Bar plot showing significant reduction in *Muribaculaceae* and *Bifidobacterium*, and increased abundance of *Helicobacter* in the MWCNTs group. A *p* value of less than 0.05 is considered significant (significance is denoted as *)

a clear separation in microbial community structure between the two groups (Fig. 9B), indicating significant alterations in microbial composition. At the phylum level, relative abundance analysis showed a notable decrease in *Bacteroidota* and an increase in *Firmicutes* following MWCNT exposure (Fig. 9C). At the genus level, the microbial community was significantly reshaped, as evidenced by changes in the abundance of key genera (Fig. 9D). LEfSe analysis identified taxa that were significantly enriched in each group. Cladogram (Fig. 9E) and LDA score (Fig. 9F) highlighted *Muribaculaceae*, *Helicobacter*, and *Bifidobacterium* as key contributors to group-specific differences. We observed a reduction in the relative abundances of *Muribaculaceae* and *Bifidobacterium*, as well as an enrichment of *Helicobacter*, in the MWCNT-exposed group compared to the Control group (Fig. 9G). *Bifidobacterium*, as a beneficial gut bacterium, can maintain an acidic environment in the gut by producing short-chain fatty acids, inhibit the growth of harmful bacteria, and regulate the gut immune response [51]. A decrease in its quantity can disrupt the balance of the gut microecology [52]. The increase in *Helicobacter* can trigger an inflammatory response in the gut [53], releasing inflammatory factors that not only affect the health of the gut itself but may also exacerbate lung inflammation through the lung-gut axis. These results suggest that MWCNT exposure leads to gut dysbiosis, which may further exacerbate systemic inflammation and epithelial barrier dysfunction.

Correlation between fecal microbiota and metabolites suggests a lung–gut axis–mediated systemic disturbance

To further explore the relationship between gut microbiota and metabolic changes induced by MWCNT exposure, we conducted fecal metabolomic analysis combined with microbial correlation assessment. Following MWCNT exposure, the fecal metabolite profiles of mice differed significantly from those of the Control group (Fig. S8). PLS-DA of the fecal metabolome identified 10 key discriminatory metabolites that contributed most to group separation, including 2-phenylethanol, quinic acid, biochanin A, quercetin, 3,4-dihydroxymandelic acid, glucosamine, 2-heptanone, and creatinine (Fig. 10A). To explore potential microbe–metabolite links, Pearson correlation analysis was performed between differentially abundant gut genera and fecal metabolites (Fig. 10C, Fig. S9). *Muribaculaceae* abundance was negatively correlated with dihydrouracil and dCMP; *Helicobacter* showed a positive correlation with dodecanedioic acid and a negative correlation with trans-cinnamoyl beta-D-glucoside; *Bifidobacterium* was negatively correlated with cholesterol and positively correlated with phenyllactate. These metabolite–microbe associations highlight potential links between gut microbial shifts and host metabolic dysregulation after MWCNT exposure. A schematic illustration summarizes the systemic consequences of MWCNT-induced lung injury along the lung–gut axis (Fig. 10B). MWCNT exposure results in elevated circulating inflammatory cytokines (IL-1β, TNF-α), increased oxidative stress markers (ROS, MDA), and altered metabolites such as S1P and amino acids. The ensuing gut inflammation and barrier disruption, characterized by reduced tight junction proteins and microbiota imbalance, may further aggravate systemic injury through microbial and metabolic signaling across organ systems.

Discussion

MWCNTs have garnered significant attention due to their exceptional mechanical, electrical, and thermal properties, positioning them as promising materials in diverse fields such as electronics, energy storage, medicine, and environmental monitoring [54–56]. However, the widespread use of nanomaterials has raised concerns about potential health risks [57–59]. In this study, our results suggest that MWCNTs induce Slamf7-Slamf7 signalling to rapidly superactivate lung macrophages, and precipitate early fibrosis and cascade inflammation–metabolic disruption along the lung–gut axis.

A growing body of evidence underscores the centrality of macrophages in mediating inflammatory responses to environmental pollutants [60]. In our spatial-transcriptomic dataset, lung regions enriched in macrophages and fibroblasts expanded by 1.6–1.7-fold after MWCNT exposure. Consistent with this, long-term aspiration studies spanning 1–80 μg per mouse report dose-dependent inflammation and fibrosis, with lower doses producing milder yet directionally consistent responses [61]. Slamf7 is a cell surface receptor that recognizes Slamf7 expressed on adjacent cells, thereby promoting macrophage pro-inflammatory cytokine production by macrophages in rheumatoid arthritis [47]. Notably, emerging particle-toxicology evidence supports a mechanistic role for Slamf7 in inhaled particle–driven lung inflammation. For example, in a silica exposure model, Slamf7 regulation was linked to macrophage autophagy dysfunction and pulmonary inflammatory outputs, and Slamf7 inhibition mitigated these responses [62]. In our study, cell-communication mapping pinpointed a Slamf7–Slamf7 loop as the dominant signal within these niches. Using siRNA knockdown in vitro, we confirmed that Slamf7 promotes the TNF-α/IL-1β burst, which leads to M1 macrophage superactivation with MWCNTs exposure. Pro-inflammatory cytokines particularly TNF-α and IL-1β activate fibroblasts and accelerate extracellular-matrix deposition, further driving the onset and progression of lung fibrosis [63]. Therefore, Slamf7 may serve as a promising target for therapeutic interventions aimed at mitigating MWCNTs-induced lung fibrosis.

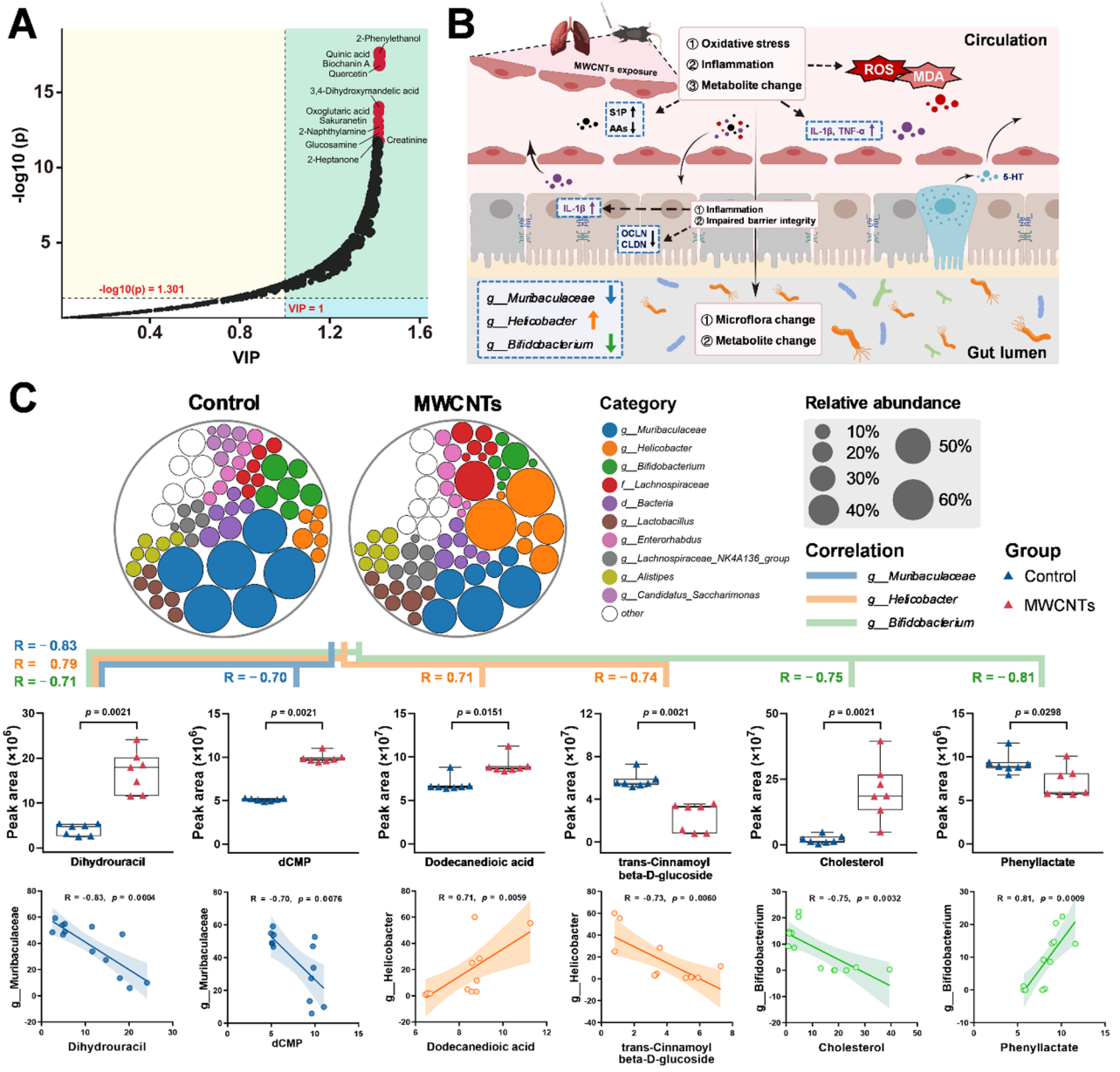

Fig. 10 Fecal metabolomic analysis and microbe–metabolite correlations after MWCNT exposure. (**A**) PLS-DA plot. (**B**) Schematic diagram illustrating the systemic effects of MWCNT exposure via the lung–gut axis. (**C**) Pearson correlation analysis between differentially abundant genera and associated fecal metabolites

Upon external stimulation, NOX2 in macrophages rapidly triggers a respiratory burst that generates abundant ROS [64]. In this study, oxidative genotoxicity, acting in concert with Slamf7-driven macrophage superactivation, synergistically amplifies the downstream inflammatory cascade. Our spatial transcriptomics data showed increased expression of Cybb and other NOX2 subunits in macrophage-rich regions of MWCNTs-exposed mouse lungs, which indicates sustained respiratory bursts and excessive ROS production. TNF-signalling plays a pivotal role in driving ROS production by alveolar macrophages [65]. In our study, large amounts of TNF-α from Slamf7-superactivated macrophages intensify the oxidative burst. The resulting oxidative stress caused DNA double-strand breaks (γ-H2AX positive), which were rapidly sensed by the Aim2 inflammasome, leading to caspase-1 activation and pyroptosis. Meanwhile, pyroptotic macrophages release mature IL-1β and IL-18, while ROS itself stabilizes NF-κB and HIF-1α signaling [66]. These signals together provide an additional wave of pro-fibrotic cues that reinforce TNF-α and IL-1β production from the Slamf7 circuit. Our results suggest that the feedback between oxidative genotoxicity and Slamf7 signaling increases cytokine production and fibroblast

activation and accelerates MWCNTs-induced lung fibrosis.

Cell-intrinsic metabolic programs are increasingly recognized as pivotal regulators of innate-immune activation and effector functions [67, 68]. In our serum metabolomic analysis, MWCNT exposure produced three tightly linked alterations. First, the bioactive sphingolipid S1P was significantly elevated in the serum of mice exposed to MWCNTs. Beyond activating NF-κB/Stat3 in macrophages, S1P engages S1PR2 on fibroblasts to potentiate TGF-β1-Smad and collagen synthesis, thereby providing a key signalling pathway from inflammation to fibrosis [69, 70]. Second, we observed an accumulation of the glycolytic intermediates fructose-1,6-bisphosphate and ribose-1,5-bisphosphate in serum with MWCNTs exposure. Although these metabolites are normally confined to the cytosol, their appearance in the circulation may signal heightened glycolytic flux combined with cell turnover or active export from strongly stimulated immune cells [71]. Consistently, *Pfkl*, *Pfkfb4* and *Tkt* transcripts were elevated in lung macrophages after MWCNTs exposure, which indicate a shift toward glycolysis and the pentose-phosphate pathway to meet the ATP demands of Slamf7-superactivated cells. Third, serine were downregulated in mice blood after MWCNT exposure. Under inflammatory conditions, reduced serine levels in the blood may cause abnormal cytokine expression in macrophages, resulting in increased pro-inflammatory factors [72]. Collectively, these lipid- and carbon-flux changes delineate an immunometabolic circuit that sustains the inflammatory program initiated by Slamf7 superactivation and simultaneously primes fibroblasts for extracellular-matrix deposition.

Together with the rise in circulating cytokines and oxidative mediators after MWCNT exposure, these serum-borne signals provide a plausible route by which lung inflammation could influence distal intestinal barrier function even when particle translocation is limited [73, 74]. Emerging evidence from our study indicates that inflammatory insults originating in the lung propagate distally to the large intestine after MWCNTs exposure. Rectal immunofluorescence in MWCNTs-exposed mice revealed reduced OCLN and CLDN1, together with focal TGF-β1 and IL-1β up-regulation, indicating a breach of epithelial tight junctions. This pattern is compatible with cytokine-mediated barrier weakening, as IL-1β can directly impair tight-junction integrity in intestinal epithelium, and systemic inflammation is increasingly recognized as a key driver of epithelial vulnerability [74, 75]. In parallel, 16S rRNA profiling showed a composition shift in the fecal microbiota, pro-inflammatory *Helicobacter* expanded, and beneficial *Bifidobacterium* and *Muribaculaceae* contracted. Untargeted metabolomics revealed a marked accumulation of ω-dicarboxylic acids alongside a pronounced depletion of phenyllactate in MWCNT-exposed mice. Notably, ω-dicarboxylic acids are peroxisomal β-oxidation products that potentiate NLRP3 inflammasome activation, whereas phenyllactate is an aryl-hydrocarbon-receptor ligand that normally restrains intestinal inflammation [76, 77]. Correlation analysis linked *Helicobacter* to ω-dicarboxylic acids and *Bifidobacterium* loss to phenyllactate depletion, suggesting that dysbiosis exports bioactive metabolites that re-enter the circulation and reinforce the systemic cytokine–ROS milieu established in the lung. Similar lung-to-gut crosstalk has been reported for chronic cigarette-smoke exposure, which remodels the colonic microbiome and promotes colorectal carcinogenesis via metabolite-mediated immune modulation [78]. These observations provide modern mechanistic support for the traditional Chinese medicine axiom that the lung and large intestine are functionally interconnected, and they point to a potentially self-reinforcing lung–gut circuit after MWCNT exposure that warrants direct mechanistic testing.

Notably, MWCNTs exert opposite effect on health under different physiological and pathological conditions. In an orthotopic breast-cancer model, pulmonary delivery of pristine MWCNTs fostered metastatic seeding by skewing macrophages toward an lncRNA-guided M2 phenotype [79]. In contrast, oxidized MWCNTs engineered to target VEGFR curtailed metastasis by disrupting microtubules in tumour and stromal cells [80]. These findings underscore the context-dependent nature of MWCNTs' biological effects, which are critically influenced by factors such as exposure route, physicochemical properties, tissue microenvironment, and immune status. Hence, precise nanomaterial design, surface modification, and targeted delivery strategies to optimize therapeutic efficacy while minimizing potential risks, ultimately facilitating the rational and safe application of carbon nanomaterials in biomedicine.

Although our single-bolus aspiration model and submerged exposure in vitro enable controlled mechanistic interrogation, they do not fully capture chronic, low-dose inhalation scenarios or air–liquid interface deposition. Future studies should adopt dosimetry-guided, inhalation-relevant regimens and acute lung injury based platforms across diverse MWCNT variants, together with Slamf7 perturbation in vivo to establish causality. Disentangling circulating mediators from potential gastrointestinal delivery routes, functionally validating microbiota–metabolite contributions, and replicating these findings in female cohorts are key future research directions to strengthen generalisability for risk assessment.

Conclusions

In conclusion, our results demonstrate that inhaled MWCNTs induced distinct spatial reorganization of pulmonary cellular architecture, characterized by macrophage- and fibroblast-enriched clusters associated with localized immune activation, and the Slamf7-driven macrophage superactivation appears to represent an important regulatory node in this process. Mechanistically, our results suggest that macrophage superactivation mediated by Slamf7 ultimately leads to lung fibrosis in MWCNTs-exposed mice by rapidly activating the Aim2 inflammasome, robustly releasing TNF-α/IL-1β, and accelerating collagen deposition. In addition, our study uncovers a pathological cycle in MWCNTs-exposed mice, whereby serum enriched with pro-inflammatory cytokines and bioactive metabolites may help propagate inflammatory and oxidative cues to the distal rectum, leading to barrier injury and local inflammation. Gut dysbiosis further exacerbates intestinal barrier damage and triggers the release of increased metabolites such as 5-HT from intestinal cells, which metabolites subsequently propagate through the bloodstream to sustain lung inflammation. This study provides mechanistic support for the traditional Chinese medicine concept of the connection between the lung and large intestine, and identifies Slamf7 signalling based on macrophage superactivation and microbiota modulation as actionable intervention points for engineering safer MWCNT formulations.

Abbreviations

MWCNTs	Multi-walled carbon nanotubes
NADPH	Nicotinamide adenine dinucleotide phosphate (reduced)
ROS	Reactive oxygen species
CNTs	Carbon nanotubes
TEM	Transmission electron microscope
H&E	Hematoxylin and eosin
SEM	Standard error of the mean
DEGs	Differentially expressed genes
CD68	Cluster of differentiation 68
Saa3	Serum amyloid A3
Gpnmb	Glycoprotein non-metastatic melanoma protein B
Mpeg1	Macrophage expressed gene 1
Cybb	Cytochrome b-245 beta chain
NOX2	NADPH oxidase 2
Cyba	Cytochrome b-245 alpha chain
Ncf1	Neutrophil cytosolic factor 1
Ncf2	Neutrophil cytosolic factor 2
Ncf4	Neutrophil cytosolic factor 4
Noxa1	NADPH oxidase activator 1
α-SMA	alpha-smooth muscle actin
FOXJ1	Forkhead box J1
FN1	Fibronectin 1
PDPN	Podoplanin
CLDN1	Claudin-1
COL1A2	Collagen type I alpha 2 chain
5-HT	5-hydroxytryptamine (serotonin)
Adgre1	Adhesion G protein-coupled receptor E1 (F4/80)
iNOS	Inducible nitric-oxide synthase
Arg1	Arginase 1
IL-1β	Interleukin-1 beta
TNF-α	Tumor necrosis factor alpha
Gsdmd	Gasdermin D
TGF-β1	Transforming growth factor beta 1
NF-κB	Nuclear factor kappa B
HIF-1α	Hypoxia-inducible factor 1-alpha
KEGG	Kyoto Encyclopedia of Genes and Genomes
GO	Gene Ontology
S1P	Sphingosine-1-phosphate
Sod3	Superoxide dismutase 3
Gpx3	Glutathione peroxidase 3
Gsta3	Glutathione S-transferase alpha 3
Adamts5	ADAM metallopeptidase with thrombospondin type 1 motif 5

Supplementary Information

The online version contains supplementary material available at https://doi.org/10.1186/s12951-026-04135-5.

Supplementary Material 1

Acknowledgements

Not applicable.

Author contributions

Biqi Han: Conceptualization, Methodology, Writing – original draft, Validation. Xinwei Li: Methodology, Data curation. Jiayi Li: Methodology. Yunfeng Liu: Supervision. Siyu Li: Visualization. Jiawen Tian: Software. Zhanjun Lv: Writing – review and editing. Dongfang Liu: Data curation. Miaomiao Li: Validation. Shuke Ji: Validation. Jingjing Lu: Writing – original draft. Zhigang Zhang: Conceptualization, Supervision, Writing – review and editing.

Funding

This work was supported by grants from the Key Projects of the Joint Fund of Heilongjiang Provincial Natural Science Foundation (JJ2024ZL0127), and the National Natural Science Foundation of China (31972754).

Data availability

No datasets were generated or analysed during the current study.

Declarations

Ethics approval and consent to participate

All animal procedures were performed in accordance with institutional guidelines and approved by the Ethical Committee for Animal Experiments of Northeast Agricultural University (Grant Number: 202305001).

Consent for publication

Not applicable.

Competing interests

The authors declare no competing interests.

Author details

[1]Present address: College of Veterinary Medicine, Northeast Agricultural University, 600 Changjiang Road, Harbin 150030, China
[2]State Key Laboratory for Zoonotic Diseases, Key Laboratory of Zoonosis Research, Ministry of Education, College of Veterinary Medicine, Jilin University, Changchun 130062, China
[3]College of Veterinary Medicine, Inner Mongolia Agricultural University, No. 29, Erdosdong Road, Saihan District, Hohhot 010011, China

Received: 30 October 2025 / Accepted: 2 February 2026
Published online: 04 March 2026

References

1. De Volder MFL, Tawfick SH, Baughman RH, Hart AJ. Carbon nanotubes: present and future commercial applications. Science. 2013;339:535–9.
2. Bai Y, Zhang R, Ye X, Zhu Z, Xie H, Shen B, et al. Carbon nanotube bundles with tensile strength over 80 GPa. Nat Nanotechnol. 2018;13:589–95.

3. Kim M, Goerzen D, Jena PV, Zeng E, Pasquali M, Meidl RA, et al. Human and environmental safety of carbon nanotubes across their life cycle. Nat Rev Mater. 2024;9:63–81.
4. Temizel-Sekeryan S, Wu F, Hicks AL. Global scale life cycle environmental impacts of single- and multi-walled carbon nanotube synthesis processes. Int J Life Cycle Assess. 2021;26:656–72.
5. Liao HY, Chung YT, Lai CH, Wang SL, Chiang HC, Li LA, et al. Six-month follow-up study of health markers of nanomaterials among workers handling engineered nanomaterials. Nanotoxicology. 2014;8:100–10.
6. Fatkhutdinova LM, Khaliullin TO, Vasil'yeva OL, Zalyalov RR, Mustafin IG, Kisin ER, et al. Fibrosis biomarkers in workers exposed to MWCNTs. Toxicol Appl Pharmacol. 2016;299:125–31.
7. Wu M, Gordon RE, Herbert R, Padilla M, Moline J, Mendelson D, et al. Lung disease in world trade center responders exposed to dust and smoke: carbon nanotubes found in the lungs of world trade center patients and dust samples. Environ Health Perspect. 2010;118:499–504.
8. Grosse Y, Loomis D, Guyton KZ, Lauby-Secretan B, El Ghissassi F, Bouvard V, et al. Carcinogenicity of fluoro-edenite, silicon carbide fibres and whiskers, and carbon nanotubes. Lancet Oncol. 2014;15:1427–8.
9. Hewitt RJ, Lloyd CM. Regulation of immune responses by the airway epithelial cell landscape. Nat Rev Immunol. 2021;21:347–62.
10. Li X, Zhang J, Wang M, Du C, Zhang W, Jiang Y, et al. Pulmonary surfactant homeostasis dysfunction mediates multiwalled carbon nanotubes induced lung fibrosis via elevating surface tension. ACS Nano. 2024;18:2828–40.
11. Scala G, Delaval MN, Mukherjee SP, Federico A, Khaliullin TO, Yanamala N, et al. Multi-walled carbon nanotubes elicit concordant changes in DNA methylation and gene expression following long-term pulmonary exposure in mice. Carbon. 2021;178:563–72.
12. Reamon-Buettner SM, Rittinghausen S, Klauke A, Hiemisch A, Ziemann C. Malignant peritoneal mesotheliomas of rats induced by multiwalled carbon nanotubes and Amosite asbestos: transcriptome and epigenetic profiles. Part Fibre Toxicol. 2024;21:3.
13. Li R, Li J, Zhou X. Lung microbiome: new insights into the pathogenesis of respiratory diseases. Signal Transduct Target Ther. 2024;9:19.
14. Liao M, Liu Y, Yuan J, Wen Y, Xu G, Zhao J, et al. Single-cell landscape of Bronchoalveolar immune cells in patients with COVID-19. Nat Med. 2020;26:842–4.
15. Grant RA, Morales-Nebreda L, Markov NS, Swaminathan S, Querrey M, Guzman ER, et al. Circuits between infected macrophages and T cells in SARS-CoV-2 pneumonia. Nature. 2021;590:635–41.
16. Liu J, Wan M, Lyon CJ, Hu TY. Nanomedicine therapies modulating macrophage dysfunction: a potential strategy to attenuate cytokine storms in severe infections. Theranostics. 2020;10:9591–600.
17. Liu B, Bing Q, Li S, Han B, Lu J, Baiyun R, et al. Role of A_2B adenosine receptor-dependent adenosine signaling in multi-walled carbon nanotube-triggered lung fibrosis in mice. J Nanobiotechnol. 2019;17:45.
18. Lee HY, You DJ, Taylor-Just A, Tisch LJ, Bartone RD, Atkins HM, et al. Role of the protease-activated receptor-2 (PAR2) in the exacerbation of house dust mite-induced murine allergic lung disease by multi-walled carbon nanotubes. Part Fibre Toxicol. 2023;20:32.
19. Ding Z, Zhong R, Yang Y, Xia T, Wang W, Wang Y, et al. Systems Pharmacology reveals the mechanism of activity of Ge-Gen-Qin-Lian Decoction against LPS-induced acute lung injury: a novel strategy for exploring active components and effective mechanism of TCM formulae. Pharmacol Res. 2020;156:104759.
20. Yiangou L, Ross ADB, Goh KJ, Vallier L. Human pluripotent stem cell-derived endoderm for modeling development and clinical applications. Cell Stem Cell. 2018;22:485–99.
21. Wang J, Xue X, Zhao X, Luo L, Liu J, Dai S, et al. Forsythiaside A alleviates acute lung injury by inhibiting inflammation and epithelial barrier damages in lung and colon through PPAR-γ/RXR-α complex. J Adv Res. 2024;60:183–200.
22. Perdijk O, Butler A, Macowan M, Chatzis R, Bulanda E, Grant RD, et al. Antibiotic-driven dysbiosis in early life disrupts indole-3-propionic acid production and exacerbates allergic airway inflammation in adulthood. Immunity. 2024;57:1939–54. .e7.
23. Tian JL, Wang N, Zhao QF, Zang ZH, Li ZY, Wang ZY, et al. Design of a sustained-release nanosystem for ultra-efficient absorption of anthocyanins and regulating lung damage through the lung-gut axis. J Adv Res. 2025. https://doi.org/10.1016/j.jare.2025.05.059.
24. Wu H, Eckhardt CM, Baccarelli AA. Molecular mechanisms of environmental exposures and human disease. Nat Rev Genet. 2023;24:332–44.
25. Barbieri M, Prattichizzo F, La Grotta R, Matacchione G, Scisciola L, Fontanella RA, et al. Is it time to revise the fighting strategy toward type 2 diabetes? Sex and pollution as new risk factors. Ageing Res Rev. 2024;99:102405.
26. Yin Y, Sichler A, Ecker J, Laschinger M, Liebisch G, Höring M, et al. Gut microbiota promote liver regeneration through hepatic membrane phospholipid biosynthesis. J Hepatol. 2023;78:820–35.
27. Özçam M, Lynch SV. The gut–airway Microbiome axis in health and respiratory diseases. Nat Rev Microbiol. 2024;22:492–506.
28. Han B, Li J, Li S, Liu Y, Zhang Z. Effects of thiacloprid exposure on microbiota–gut–liver axis: multiomics mechanistic analysis in Japanese quails. J Hazard Mater. 2023;442:130082.
29. Liu D, Song K, Li M, Han B, Lv Z, Li J, et al. Polystyrene microplastics modulation of hexavalent chromium toxicity in quails: transcriptomic and toxicological insights. Environ Chem Ecotoxicol. 2026;8:794–809.
30. Han B, Tian J, Li J, Chen Y, Liu N, Ma Y, et al. Cardioprotective effects of dendrobium officinale polysaccharides on thiacloprid-induced cardiac injury via modulating mitochondrial dynamics. Int J Biol Macromol. 2025;309:142497.
31. Li J, Guo C, Liu Y, Han B, Lv Z, Jiang H, et al. Chronic arsenic exposure-provoked biotoxicity involved in liver–microbiota–gut axis disruption in chickens based on multi-omics technologies. J Adv Res. 2025;67:373–86.
32. Han B, Wang X, Wu P, Jiang H, Yang Q, Li S, et al. Pulmonary inflammatory and fibrogenic response induced by graphitized multi-walled carbon nanotube involved in cGAS-STING signaling pathway. J Hazard Mater. 2021;417:125984.
33. Han B, Li S, Lv Y, Yang D, Li J, Yang Q, et al. Dietary melatonin attenuates chromium-induced lung injury via activating the Sirt1/Pgc-1α/Nrf2 pathway. Food Funct. 2019;10:5555–65.
34. Di Ianni E, Erdem JS, Møller P, Sahlgren NM, Poulsen SS, Knudsen KB, et al. *In vitro-in vivo* correlations of pulmonary inflammogenicity and genotoxicity of MWCNT. Part Fibre Toxicol. 2021;18:25.
35. Yang Q, Han B, Li S, Wang X, Wu P, Liu Y, et al. The link between deacetylation and hepatotoxicity induced by exposure to hexavalent chromium. J Adv Res. 2021;35:129–40.
36. Wei C, Yang C, Wang S, Shi D, Zhang C, Lin X, et al. Crosstalk between cancer cells and tumor associated macrophages is required for mesenchymal Circulating tumor cell-mediated colorectal cancer metastasis. Mol Cancer. 2019;18:64.
37. Ni T, Jiao F, Yu X, Aden S, Ginger L, Williams SI, et al. Structure and mechanism of bactericidal mammalian perforin-2, an ancient agent of innate immunity. Sci Adv. 2020;6:eaax8286.
38. Lee JY, Hall JA, Kroehling L, Wu L, Najar T, Nguyen HH, et al. Serum amyloid A proteins induce pathogenic Th17 cells and promote inflammatory disease. Cell. 2020;183:2036–9.
39. Zhang Q, He Y, Luo N, Patel SJ, Han Y, Gao R, et al. Landscape and dynamics of single immune cells in hepatocellular carcinoma. Cell. 2019;179:829–e84520.
40. Kuntic M, Oelze M, Steven S, Kröller-Schön S, Stamm P, Kalinovic S, et al. Short-term e-cigarette vapour exposure causes vascular oxidative stress and dysfunction: evidence for a close connection to brain damage and a key role of the phagocytic NADPH oxidase (NOX-2). Eur Heart J. 2020;41:2472–83.
41. Amara N, Cooper MP, Voronkova MA, Webb BA, Lynch EM, Kollman JM, et al. Selective activation of PFKL suppresses the phagocytic oxidative burst. Cell. 2021;184:4480–e449415.
42. Liu X, Shi Y, Liu R, Song K, Chen L. Structure of human phagocyte NADPH oxidase in the activated state. Nature. 2024;627:189–95.
43. Jamsen JA, Sassa A, Perera L, Shock DD, Beard WA, Wilson SH. Structural basis for proficient oxidized ribonucleotide insertion in double strand break repair. Nat Commun. 2021;12:5055.
44. Xu Y, Li C, Yin H, Nowsheen S, Xu X, Kang W, et al. STK39-mediated amplification of γ-H2A.X promotes homologous recombination and contributes to PARP inhibitor resistance. Nucleic Acids Res. 2024;52:13881–95.
45. Wang C, Zhao M, Bin P, Ye Y, Chen Q, Tang Z, et al. Serine synthesis controls mitochondrial biogenesis in macrophages. Sci Adv. 2024;10:eadn2867.
46. Fu J, Han Z, Wu Z, Xia Y, Yang G, Yin Y, et al. GABA regulates IL-1β production in macrophages. Cell Rep. 2022;41:111770.
47. Simmons DP, Nguyen HN, Gomez-Rivas E, Jeong Y, Jonsson AH, Chen AF, et al. SLAMF7 engagement superactivates macrophages in acute and chronic inflammation. Sci Immunol. 2022;7:eabf2846.
48. Pellegrini JM, Keriel A, Gorvel L, Hanniffy S, Arce-Gorvel V, Bosilkovski M, et al. SLAMF7 and SLAMF8 receptors shape human plasmacytoid dendritic cell responses to intracellular bacteria. J Clin Invest. 2025;135:e182467.
49. Andersen JV, Skotte NH, Christensen SK, Polli FS, Shabani M, Markussen KH, et al. Hippocampal disruptions of synaptic and astrocyte metabolism are

primary events of early amyloid pathology in the 5xFAD mouse model of alzheimer's disease. Cell Death Dis. 2021;12:954.
50. Wei X, Qian W, Narasimhan H, Chan T, Liu X, Arish M, et al. Macrophage peroxisomes guide alveolar regeneration and limit SARS-CoV-2 tissue sequelae. Science. 2025;387:eadq2509.
51. Larke JA, Heiss BE, Ehrlich AM, Taft DH, Raybould HE, Mills DA, et al. Milk oligosaccharide-driven persistence of *Bifidobacterium* pseudocatenulatum modulates local and systemic microbial metabolites upon synbiotic treatment in conventionally colonized mice. Microbiome. 2023;11:194.
52. Nakajima A, Arzamasov AA, Sakanaka M, Murakami R, Kozakai T, Yoshida K, et al. *In vitro* competition with *Bifidobacterium* strains impairs potentially pathogenic growth of clostridium perfringens on 2'-fucosyllactose. Gut Microbes. 2025;17:2478306.
53. Vakil N. Peptic ulcer disease: a review. JAMA. 2024;332:1832–42.
54. Li X, Yang R, Zou L, Zheng S, Chen M, Wen J, et al. Reassessing the role of thermal convection in simultaneous water production and pollutant degradation in interfacial photothermal-photocatalytic systems. Adv Mater. 2025;37:e2416283.
55. Hevia LG, Fanarraga ML. Microtubule cytoskeleton-disrupting activity of mwcnts: applications in cancer treatment. J Nanobiotechnol. 2020;18:181.
56. Wu L, Du Z, Liu W, Duan Z, Liu H, Li L, et al. Crack-enhanced MXene-carbon nanotube soft contact lens for body-induced intracranial pressure application. ACS Nano. 2025;19:13128–38.
57. Bartone RD, Tisch LJ, Dominguez J, Payne CK, Bonner JC. House dust mite proteins adsorb on multiwalled carbon nanotubes forming an allergen Corona that intensifies allergic lung disease in mice. ACS Nano. 2024;18:26215–32.
58. Wan S, Wang X, Chen W, Xu Z, Zhao J, Huang W, et al. Polystyrene nanoplastics activate autophagy and suppress trophoblast cell migration/invasion and migrasome formation to induce miscarriage. ACS Nano. 2024;18:3733–51.
59. Soenen SJ, Parak WJ, Rejman J, Manshian B. (Intra)cellular stability of inorganic nanoparticles: effects on cytotoxicity, particle functionality, and biomedical applications. Chem Rev. 2015;115:2109–35.
60. Fusco L, Gazzi A, Giro L, Schefer RB, D'Almeida SM, Cagliani R, et al. Nanoplastics: immune impact, detection, and internalization after human blood exposure by single-cell mass cytometry. Adv Mater. 2025;37:e2413413.
61. Snyder-Talkington BN, Dong C, Porter DW, Ducatman B, Wolfarth MG, Andrew M, et al. Multiwalled carbon nanotube-induced pulmonary inflammatory and fibrotic responses and genomic changes following aspiration exposure in mice: A 1-year postexposure study. J Toxicol Environ Health A. 2016;79:352–66.
62. Yin H, Gu P, Xie Y, You X, Zhang Y, Yao Y, et al. ALKBH5 mediates silica particles-induced pulmonary inflammation through increased m6A modification of Slamf7 and autophagy dysfunction. J Hazard Mater. 2024;462:132736.
63. Narasimhan H, Cheon IS, Qian W, Hu SS, Parimon T, Li C, et al. An aberrant immune-epithelial progenitor niche drives viral lung sequelae. Nature. 2024;634:961–9.
64. Kim JS, Liu L, Kant S, Orlicky DJ, Uppalapati S, Margolis A, et al. Anaerobic respiration of host-derived methionine sulfoxide protects intracellular Salmonella from the phagocyte NADPH oxidase. Cell Host Microbe. 2024;32:411–e42410.
65. Arias AA, Neehus AL, Ogishi M, Meynier V, Krebs A, Lazarov T, et al. Tuberculosis in otherwise healthy adults with inherited TNF deficiency. Nature. 2024;633:417–25.
66. Zhu J, Huang S, Li Y, Xu J, Chen R, Guo M, et al. NF-κB1 p50 stabilizes HIF-1α protein through suppression of ATG7-dependent autophagy. Cell Death Dis. 2022;13:1076.
67. Li S, Duan Y, Luo S, Zhou F, Wu Q, Lu Z. Short-chain fatty acids and cancer. Trends Cancer. 2025;11:154–68.
68. Holendová B, Šalovská B, Benáková Š, Plecitá-Hlavatá L. Beyond glucose: the crucial role of redox signaling in β-cell metabolic adaptation. Metabolism. 2024;161:156027.
69. Ma Y, Zhang X, Xuan B, Li D, Yin N, Ning L, et al. Disruption of CerS6-mediated sphingolipid metabolism by FTO deficiency aggravates ulcerative colitis. Gut. 2024;73:268–81.
70. Baweja S, Kumari A, Negi P, Tomar A, Tripathi DM, Mourya AK, et al. Hepatopulmonary syndrome is associated with low sphingosine-1-phosphate levels and can be ameliorated by the functional agonist Fingolimod. J Hepatol. 2023;79:167–80.
71. Wang J, Wu Q, Qiu J. Accumulation of Fructose 1,6-bisphosphate protects clear cell renal cell carcinoma from oxidative stress. Lab Invest. 2019;99:898–908.
72. Kurita K, Ohta H, Shirakawa I, Tanaka M, Kitaura Y, Iwasaki Y, et al. Macrophages rely on extracellular Serine to suppress aberrant cytokine production. Sci Rep. 2021;11:11137.
73. Mostovenko E, Canal CG, Cho MJ, Sharma K, Erdely A, Campen MJ, et al. Indirect mediators of systemic health outcomes following nanoparticle inhalation exposure. Pharmacol Ther. 2022;235:108120.
74. Neurath MF, Artis D, Becker C. The intestinal barrier: a pivotal role in health, inflammation, and cancer. Lancet Gastroenterol Hepatol. 2025;10:573–92.
75. Rawat M, Nighot M, Al-Sadi R, Gupta Y, Viszwapriya D, Yochum G, et al. IL1B increases intestinal tight junction permeability by up-regulation of MIR200C-3p, which degrades occludin mRNA. Gastroenterology. 2020;159:1375–89.
76. Zhang W, Zhang L, Yao H, Wang Y, Zhang X, Shang L, et al. Long-chain Dicarboxylic acids play a critical role in inducing peroxisomal β-oxidation and hepatic triacylglycerol accumulation. J Biol Chem. 2023;299:105174.
77. Gao Y, Liu KY, Xiao W, Xie X, Liang Q, Tu Z, et al. Aryl hydrocarbon receptor confers protection against macrophage pyroptosis and intestinal inflammation through regulating polyamine biosynthesis. Theranostics. 2024;14:4218–39.
78. Bai X, Wei H, Liu W, Coker OO, Gou H, Liu C, et al. Cigarette smoke promotes colorectal cancer through modulation of gut microbiota and related metabolites. Gut. 2022;71:2439–50.
79. Ding K, Zhu Y, Lang Y, Zhu L, Zhang TT, Zhang R, et al. Multiwalled carbon nanotubes-reprogrammed macrophages facilitate breast cancer metastasis via NBR2/TBX1 axis. ACS Nano. 2024;18:11103–19.
80. García-Hevia L, Soltani R, González J, Chaloin O, Ménard-Moyon C, Bianco A, et al. Carbon nanotubes targeted to the tumor microenvironment inhibit metastasis in a preclinical model of melanoma. Bioact Mater. 2024;34:237–47.

Publisher's note